3D PRINTING OF ENERGETIC MATERIAL

A Thesis

Presented to

the Faculty of the University of

at the University of Missouri - Columbia

In Partial fulfillment
of the Requirements for the Degree

Master of Science

By

Andrew Countryman

Dr. Matthew Maschmann, Thesis Supervisor

MAY 2019

The undersigned, appointment by the Dean of the Graduate School have examined the

thesis entitled

3D Printing of Energetic Materials

Presented by Andrew Countryman
a candidate for the degree of Master of Science
and here by certify that in their opinion it is worthy of acceptance.

_____

Dr. Matthew Maschmann, Chair

_____

Dr. Jacob McFarland

_____

Dr. Stephen Montgomery - Smith

ACKNOWLEDGEMENTS

TABLE OF CONTENTS

LIST OF FIGURES

LIST OF TABLES

3D PRINTING OF ENERGETIC MATERIAL

Andrew Countryman

Dr. Matthew Maschmann, Thesis Supervisor

In the world of macro-scale energetics, the problems of cost effectiveness, scalability, and manufacturability are of prime importance. But with the advent of 3D printing, a solution for scalability is in reach. In this work, THV and GO are explored as candidate materials for printing. To avoid subjectivity, the materials have to pass a test of repeatability, control of geometry, and layer building. Moreover, a novel drop on demand 3D printing system was explored as the printing method. The overall goal is to take the material out of the lab room and into a scalable manufacturing technique. After initial testing, it was decided that THV is suitable for 3D printing while GO needs to be developed further to enable printability.

Chapter 1- Introduction

1.1. Additive Manufacturing

Additive Manufacturing (AM), or 3D Printing (3DP) is a collection of material processing methods that create desired shapes by the continuous addition of material to "build" an object. Typically, material is added to a component using a layer-by-layer deposition process. Unlike subtractive manufacturing methods like lathing, milling, and CNC, AM builds geometry from the bottom up, enabling the production of complicated geometries. The process enables the use of a wide spectrum of materials including polymers, metals, and ceramics. Current research is broadening the set of materials compatible with 3DP while increasing print resolution and speed.

At its infancy, this technology was used as a means to create tangible prototypes of designs. The first 3D printer used stereolithography (SLA) technology to draw and solidify each layer of a part in a UV-sensitive resin [1]. To build a layer, the laser interacted with the resin pool and locally cured to the previous layer or to the build plate. The laser was rastered through a projection system to rapidly cure (harden) the resin upon exposure. Upon completion of one layer, a platform piston would drop the component deeper into the resin by a displacement equal to the build height. The process would then repeat layer by layer. Each layer had a resolution approximately the same as of the laser impact size (on the order of 25-100 micron). To facilitate a reliable print, the system heavily relied on a level pool for the resin and a level build platform. Thus, these early systems were susceptible to even the smallest perturbations during the print process.
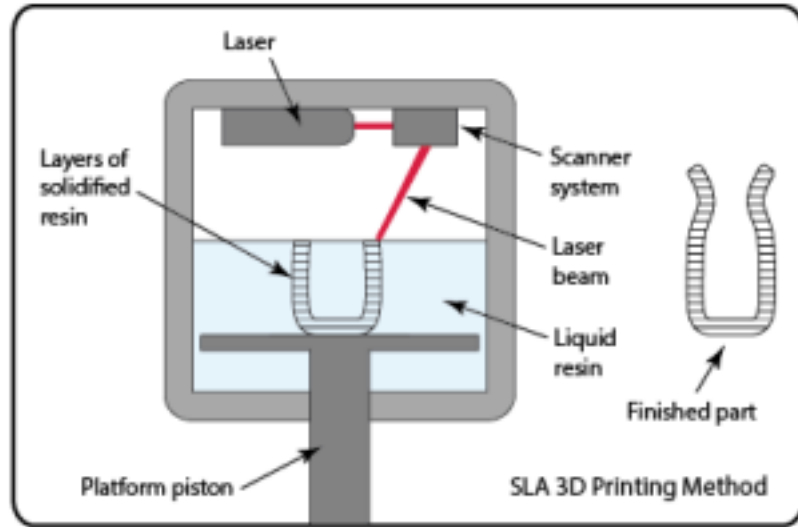
Figure 1 – Schematic of a sterolithograpy printer. The system consists of a photo-sensitive resin bath that is locally cured upon contact with a laser of appropriate wavelength. The cured layers accumilate for the final 3D componenet. [2]

Any disturbance of early SLA would catastrophically disrupt the print, and widespread adoption of these systems was not accomplished except for specialized prototyping. To combat this, Stratasys devised the fused deposition modeling (FDM) technology 1991. Instead of relying on the curing of a photosensitive resin bath, this technology utilized computer numerical control (CNC) technology to control the path of an extrusion tool (extruder) above the build platform. Thermoplastic filaments (mainly ABS and PLA plastics) are fed into the extruder head at room temperature. The filaments are then heated to a molten state in the same manner as a hot glue gun and extruded onto a build platform to re-solidify. As seen in Figure 2, this technique builds print components from the bottom up layer by layer.
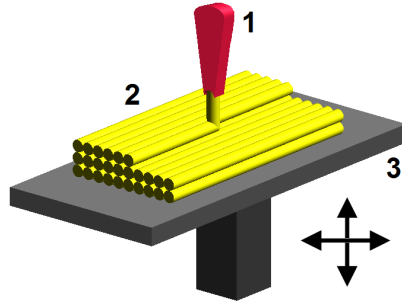
Figure 2 – Schematic of the fused deposition method (FDM) printing method. The system consists of (1) a heated extrution head through which molton thermoplastic is extruded as (2) deposited material layers. The molten thermoplastic is depositied on(3) a build plate. [3]

Knowing the proper deposited filament height and width is critical to a proper build with the FDM method. These factors are controlled by the diameter of the extruder orifice, the feed rate of the filament through the extruder, the rate at which the extruder translates above the build plate, the extruder's temperature, and melting point of the filament. Based upon the proper width and height of the deposited filament, a computer program called a slicer is used to determine the path of the heated nozzle required to deposit the 3D elements. Upon completion of one layer, the nozzle traces the path corresponding to the next printed layer, creating a three-dimensional object one layer at a time. Normal FDM printing has a minimum print height per layer of 100-500 micron, which was a noticeable increase relative to the SLA printers. The increased print height facilitated a drastic decrease in build time

But while SLA and FDM relied on curable resin and thermoplastics, respectively, selective laser sintering (SLS) was the first technique to successfully print in a wide range of materials. Developed in the University of Texas at Austin by Dr. Carl Deckard and Dr. Joe Beaman, this method utilizes a thermal laser to locally melt and/or sinter a powdered material [4].

Selective Laser Sintering

1 Heaters
2 Build Chamber
3 Powder Delivery System
4 Printed part
5 Recoater
6 Laser Beam
7 X-Y Scanning Mirror
8 Laser
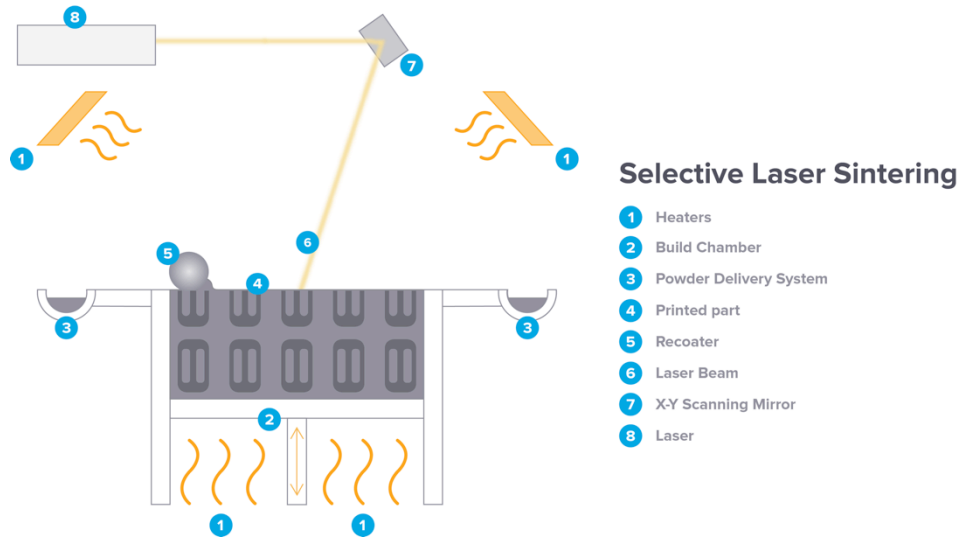
Figure 3 - Schematic of the selective laser sintering (SLS) printing method.

Overall, the approach is very similar to the SLA method. In both, a laser is strategically directed to cure/melt the desired material, thus creating an overall resolution of 25-100 micron, similar to SLA. This is where the similarity ends. When a layer is complete, the SLS machine lowers the build chamber by a desired layer height and a powder delivery service coats the top of the chamber with a new powder layer. Because the material is in powder form during the print, any unused powder can be reclaimed and recycled for future prints. Moreover, the laser can be adapted to melt a range of powders, including glass, plastics, ceramics, and metals. [4]. Although boasting the most expansive material resume, this method has been historically very expensive. This is currently the main drawback for the average consumer.

With the advent of all of these new methods, it was colossal "news to inventors, who could now theoretically prototype and test their designs without having to make a huge upfront investment in manufacturing" [5]. Traditional machining methods require large investments for the costs of molds, tooling, raw materials, and/or equipment. These methods

4

create permanent solutions and are amenable for mass production. But if a design is still changing, the extra cost is not justified when only one or two prototypes are made. 3D printing creates the option of a cheaper alternative to the traditional methods. With a single printer, inventors can create a highly resolved prototype in a short amount of time and have the flexibility to update their design and have another prototype with very little turnaround. The turnaround time from design to delivery of a prototype is the only time to finish the print. The same equipment set with no additional cost or time to re-tool may manufacture distinctly different parts

SD3D, an additive manufacturing company with injection molding experience explored the costs between the injection molding versus 3DP set quantities of 12-ounce soda cans [6]. Table 1 highlights their findings.

Table 1 – Case study of SD3D printing and Injection Molding [6]

MANUFACTURING 12 OUNCE SODA CANS

SD3D VS INJECTION MOLDING

QTY	INJECTION MOLDING	SD3D*
100	$35,552.00 $355.52 PER UNIT	$2,942.94 $29.43 PER UNIT
500	$36,591 $73.18 PER UNIT	$10,208.11 $20.42 PER UNIT
1,000	$37,888 $37.89 PER UNIT	$18,917.22 $18.92 PER UNIT
5,000	$48,276 $9.66 PER UNIT	$48,238.07 $9.65 PER UNIT

*AT STANDARD SETTINGS

In their project, the injection molding required a single tooling cost of $34,983 to begin manufacture. Including the cost of material, each unit will have to share this cost throughout the run cycle. Thus, the overall cost per unit drastically decreases as the overall quantity increases, proving that injection molding is viable in very large production runs. But,

if there is any change to the desired design, this initial cost will have to be paid again.
Compared to 3D printing through SD3D, the small unit quantities have a major advantage.
Instead of a once per run tooling fee, printing with SD3D has a flat yearly rate averaged at
$1,000. This includes the use of the printers, man-hours, and a material cost of $0.18 per cubic
inch. This flexible payment structure allows for a multitude of design changes to a model
without the recurring tooling fee. This, and the much lower entry cost are perfectly suited for
short production runs, or even a handful of an inventor's prototypes. Even for the large
quaintly of 100 cans, SD3D's AM cost 8% of the overall cost of injection molding. This is a
huge incentive to use 3D printing in small batch printing.

As AM begins to mature, the technology is being to be applied to a host of new
material sets and applications. This is most evident by the rapid growth of academic
publications in the area. Figure 4 shows the number of publications in 3DP by year. The plot
was generated using Web of Science using the search term "3D printing". After a slow rise
from the mid 1990's to 2010, the number of publications increased nearly exponentially over
the succeeding years.
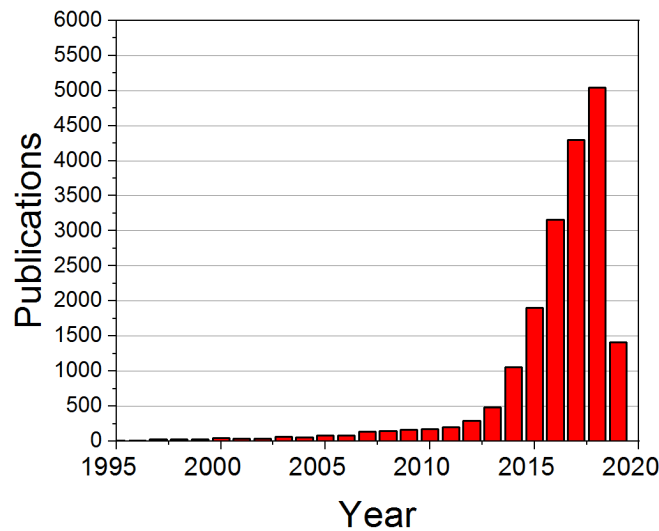
Figure 4 – Number of publications on the topic of "3D Printing" [7]

With the explosion of research being conducted in the field of 3D printing, the

technology can be seen being applied to countless subjects. Just to highlight a few, the

technology is breaking grounds in the Biomedical community. Scientists in Tel Aviv, Israel

broken ground on 3D printing cardiac tissue using human stem cells. Published in the Journal

of Advanced Sciences, their article, *3D Printing of Personalized Thick and Perfusable*

Cardiac Patches and Hearts, lays the groundwork for the creation of specialized bioink and

the process of printing complicated cardiac organs. [8] Through a novel cultivation,

reprogramming, and hydrogel synthesis method, they created two models, a proof of concept

for patient specific treatment, and another for large-scale printing/experimentation [8].

Through the use of CT scans, a cardiac blood cell patch was converted into a 3D model, and

then was successfully printed into support median/well. Ultimately, the 3D tissue printed

proved to be fully matched in "anatomical structure as well as the biochemical and cellular

components of any individual". Thus, the personalization of bio-printed organs is within

reach. If fully reached, the rejection rate of new organs will plummet since these specific organs are printed using the patients' individual cells. The next goal is to scale experimentation to large organs and engineer methods to preserve the expansive cell cultures needed to print these organs.

Moreover, 3D printing is beginning to be a major contributor to Civil Engineering. A few current achievements and companies are highlighted in the article, *3D Printing of Buildings and Building Components as the Future of Sustainable Construction?* [9]. In it, they highlight two methods of novel building methods, a method the WinSun Company used to 3D print "building elements" inside of their factory, and then assemble the building blocks on site. Although the building material is larger, the assembly of these modules is much simpler to complete. Moreover, buildings can be designed through the use of these blocks, simplifying the logistics and architectural design of these buildings. Also, the use of "In-site Contour Crafting (CC)" is described as the "most promising" method to be used in the civil industry [9]. Through the use of expansive Cartesian printers that mix concrete with sand, buildings can be extruded on site. In a method that is very similar to FDM, the technology has already been applied in the creation of Andy Rudenko's castle, seen in Figure 5. This castle is a fantastic proof of concept for the strength of the technology.

Figure 5 – Andy Rudenko's concrete castle [9].

Within this document, we thoroughly analyzed the material properties and printability of THV and graphene oxide aerogel. The material sets are of specific importance to the field of nanothermite material research. A major constraint of working with nanothermites is that material processing must be minimally intrusive. To preserve the thermal and explosive potentials of these materials, nothing can be introduced to the original material. To reduce subjectivity in deciding the printability of each material, a certification process must be established. To certify a material, it must check 3 criteria: repeatability, control of geometry, and ability to print multiple layers. To achieve repeatability, the material must be able to successfully print the first layer of a print 3 or more times without major error. For control of geometry, the material must be able to control the final shape of the print. And to pass multiple layers, the material must be able to build distinct layers above the first. It is important to note that although the final goal of 3D printing these materials is to construct nanoenergetic materials (including fuel and oxidizer nanoparticles), all testing contained within this document uses an inert version of THV and GO, lacking any aluminum nanoparticle fuel. This facilitates safe experimentation as we explore the base materials and the printing process.

1.2. Material Introduction

1.2.1. Graphene Oxide

Graphene is a 2-D material that is presently being explored for its excellent thermal, mechanical, and electrical properties. Because graphene is comprised of a single atomic layer, all atoms reside on the surface of the material. Surprisingly, the first isolation of a graphene layer from bulk graphite was achieved in using scotch tape to successively exfoliate thinner and thinner layers. The achievement of isolating a 2D material was awarded the Nobel Prize in physics in 2010 [10]. Since the exfoliation process of graphene was demonstrated, many research groups have successfully synthesized high-quality graphene using the chemical vapor deposition (CVD) process [11].
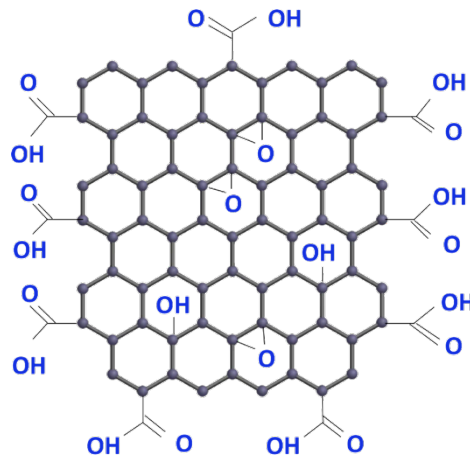
Figure 6. A schematic of the molecular structure of GO. [12]

Graphene oxide (GO) is closely related to graphene; however, graphene oxide is intentionally functionalized with oxidative chemical species. The synthesis of GO typically follows the Hummers Method [13]. In this method, graphite powder is exfoliated via sonication in H_2SO_4 with K_2FeO_4 and $KMnO_4$. After 6 minutes, $KMnO_2$ is added while the

solution was heated to 90 °C. After a half an hour, deionized water was added and the solution was allowed to cool. Once cool, impurities were removed through a lengthy washing cycle. This cycle included introducing fresh water to the solution, a centrifugal and diffusion step, then pipetting impure water out of the system. Once the GO reached 6 pH, it was reintroduced into distilled water and sonicated. This step exfoliates the powder into thin sheets. The material is then placed into an oven, where the deionized water is evaporated, leaving behind the thin sheets of GO. The process functionalizes the material with hydroxyl species and other oxidizers. A schematic of GO is shown in Figure 6. The terminal step in the production of GO is typically the rinsing and drying of the material to form a bulk powder.
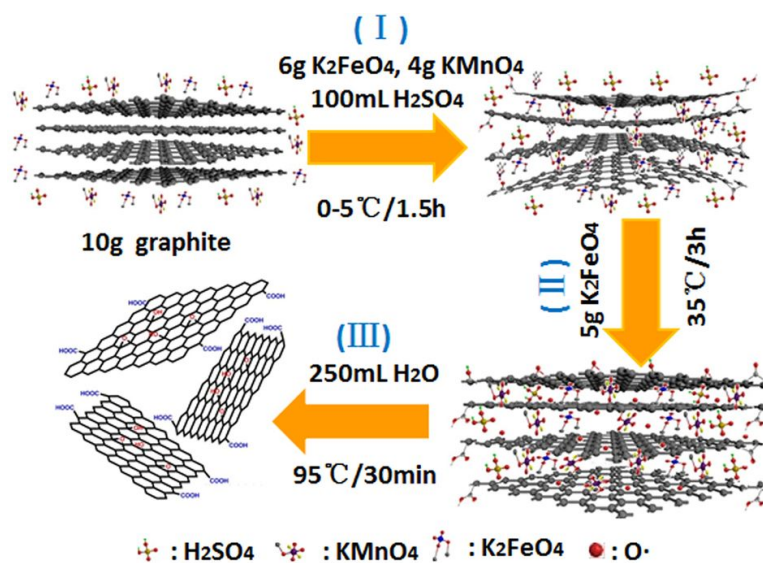
Figure 7. Schematic of Hummers Method. [13]

In the energetics community, GO and chemically reduced GO are of interest for their 2D structural properties [14]. In particular, the material may be used as a template for the dense self-assembly of nanothermite materials. To prepare GO-templated nanothermite material, GO and aluminum nanoparticles (Al NPs) were ultrasonically mixed in a 1:1 ratio of

DMF:IPA. The mixing induced a negative surface charge on the GO particles and a positive

surface charge on the Al NPs. When the two dispersions were mixed, the electrostatic

attraction between GO and the Al NPs led to the decoration of Al NPs on the GO particle

surface. Further, mixing the GO/Al NP dispersion with BiO_2 NPs led to a homogeneous

mixture of Al and BiO_2 NPs decorated on the surface of GO sheets. This phenomenon reduces

phase separation of thermite fuel and oxide, leading to a more efficient combustion.

Furthermore, decorated sheets further self-assembled into densely packed, layer-upon-layer

assemblies.
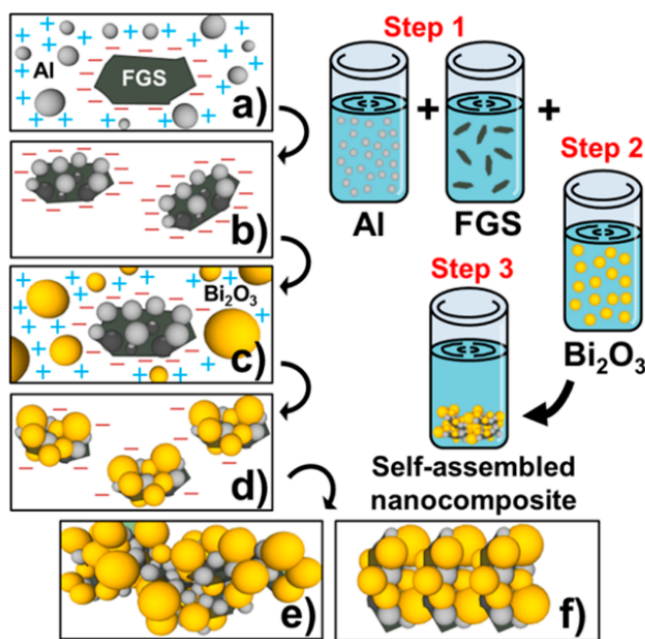
Figure 8. Self Assembly method for GO nanothermite. [14]

GO sheets may also be used to create low-density nanothermite aerogels [15]. Here,

the GO again provides a structural template for assembly of nanoscale AL and $Bi2O_3$

nanoparticles; however, the decorated GO sheets are not encouraged to self-assembly into a

dense mass. Rather, the GO sheets are encouraged to cross link while in a liquid suspension to

form a low-density gel. By itself, a dispersion of Al, Bi_2O_3, and GO sheets is not sufficient to create an aerogel. As stated in the paper, the decorated GO "requires chemical reduction and gelling [while] preserving the reactivity of the embedded fuel and oxide nanoparticles" [15]. Most chemical gelling agents are either oxidative or reductive in nature. An oxidizing agent would passivate the Al fuel, while a reducing agent would convert the solid oxide particles to metallic particles. The gelation method cannot interfere with the explosive properties of the energetic nanoparticles; thus, a novel single-step technique was developed. Here, Ethylenediamine (EDA) was used as reducing agent to chemically gel the solution. This chemical is easy to remove after reduction, and does not interfere with the energetic properties of the nanoparticle additives. For this paper, this method of reduction was used to synthesize the graphene oxide aerogel thermite material.
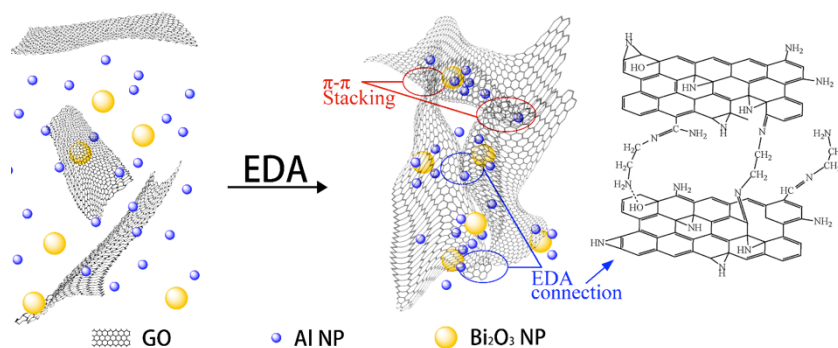
Figure 9 – EDA reduction method for GO aerogels. [15]

Research has been conducted in the synthesis of neat graphene oxide material without the use of the EDA reduction. This conventional method denoted in the article, *3D Printing of Graphene Aerogels* [16] introduces water to the GO solution. The GO is directly printed through a pneumatic drop-on-demand extruder onto a cold plate. On contact, the water-based solution freezes in place. This creates a controllable line that can withhold multiple layers.

While printing, a second extruder is used to strategically dispense extra water. This water freezes on contact, acting as a support for the next layer. After the print is complete, a lengthy freeze-drying cycle in liquid nitrogen removes water from the GO of impurities, leaving the 3D structure intact.
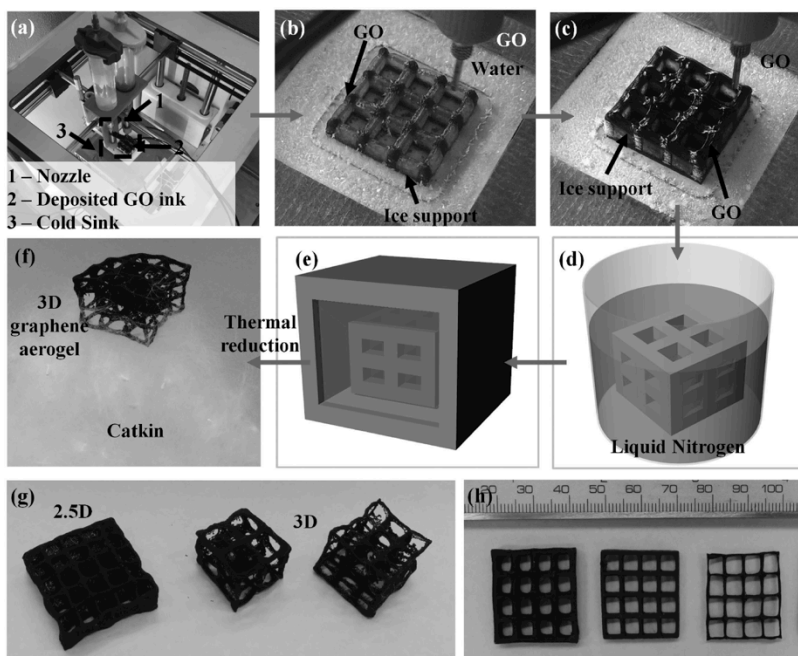
**Figure 10 – 3D printing graphene aerogel (GA). a–f) The 3D GA printing process. a) 3D printing setup. b) 3D printing of ice support. c) 3D printing
of GO suspension. d) Immersing printed ice structure into liquid nitrogen. e) Freeze drying. f) Thermally reduced to 3D ultralight GA on catkin.
g) 3D GA architecture, left: 2.5 structure and right: 3D architecture with overhang structures. h) GAs with various wall thickness. [16]**

Although straightforward, this method of printing cannot be used in conjunction with the energetic nanoparticles in mind. Any water present in the material oxidizes and passivates the Al fuel. To avert this, two inks must be printed; the GO acted as a base, and EDA as a binder, gelling each layer before moving to the next. The concentration of EDA must be tailored so that the speed of gelation and excess EDA is balanced. The greater the concentration of EDA, the faster the gelation process, but the more EDA needed to be

removed after printing. This can be accomplished through a solution swap process, where the excess EDA and any unreacted GO is swapped with Tert Butyl.

1.2.2. THV

THV, or the terpolymer of tetrafluoroethylene, hexafluoropropylene, and vinylidene-fluoride, is a polymer that is renowned for its chemical resistance, ability to be bonded to itself, and optical transparency. THV is closely related to PTFE, also known by its trade name, Teflon.
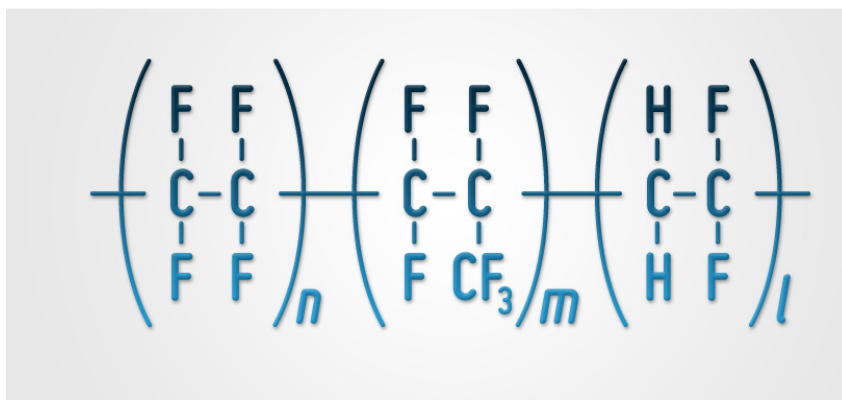
Figure 11 – THV molecular structure [17]

Used extensively in the optics and tubing industries, this material has been used to create transparent thermite materials by embedding aluminum nanoparticles into THV diluted with acetone. When the embedded AL NPs are heated (frequently using laser heating), the fluorine contained within the THV reacts with the Al fuel to create a highly exothermic reaction in which biocidal fluorine gas is released. For this reason, THV studied in the article, *Ultra-rapid elimination of biofilms via the combustion of a nanoenergetic coating* is used to create an energetic film to clean microorganisms on sensitive surfaces [18]. Described as

biofilm, these organisms can be difficult to clean off in a safe and efficient manner. THV with

Al nanoparticles can be easily sprayed onto biofilm for testing. The concentration of Al, THV

and acetone were evaluated with ignition tests as well as SEM micrographs of the biofilm

before and after the test [18]. First, biofilm was grown on 4 different substrates SEM and

normal photography can be seen in Figure 12. Notice that there are some small white

particles in the clean SEM pictures. Once the biofilm is introduced, the SEM pictures gain a

lot more texture on the surface of the substrates.
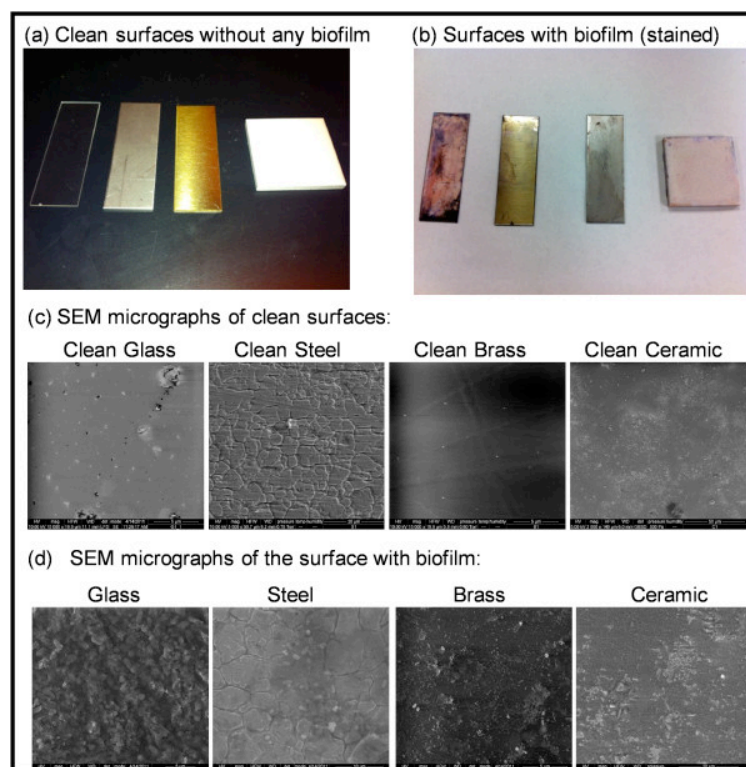
Figure 12 – Pre burn samples. SEM micrograms were taken of 4 different substrates while clean and once "stained" with the biofilm. [18]

Once the samples are ready for the THV nanoenergetic, the material was spray–coated

in an even coat layer on each sample. After a few moments to dry, the nanoenergetic was

burnt off through a flame test. The results of the flame test are seen in Figure 13. Here, a

SEM was taken directly afterwards. The biofilm successfully burnt and deformed into small portions. These portions were then washed away, leaving a no biofilm behind. Although the authors state that the process is imperfect, the uniform spray proved efficient in cleaning the biofilm off of the substrates [18].
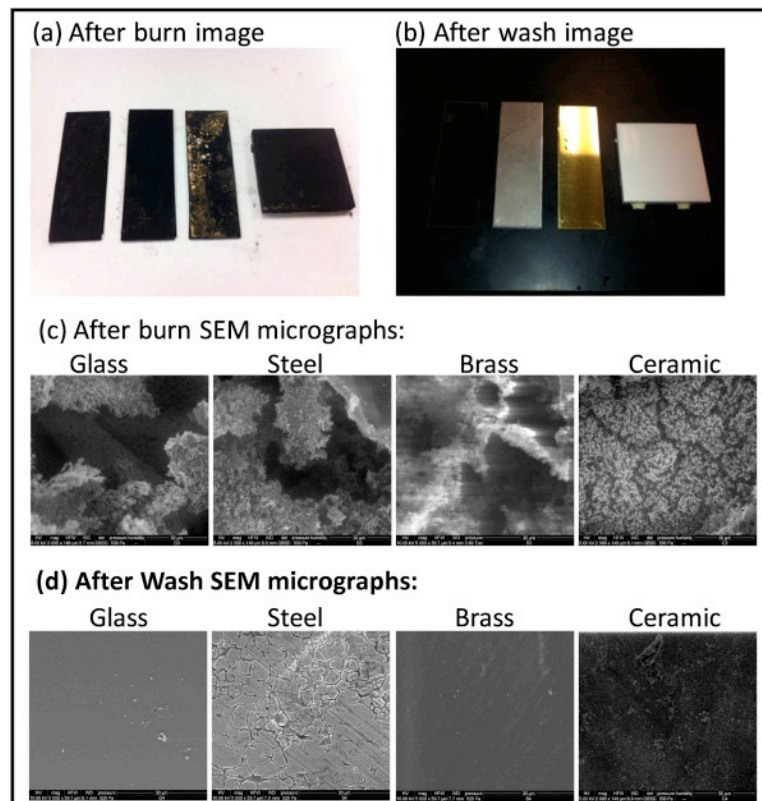
Figure 13 – After burn samles. SEM micrographs were taken directly after the burn test, and after a wash. [18]

Chapter 2- Material Development

2.1. THV

The printable THV solution consists of a two-part mixture of acetone and THV. Prior to printing, THV powder was dissolved fully in acetone at various concentrations. Preparation of the THV solution followed the same method stated in the article, *Ultra-rapid elimination of biofilms via the combustion of a nanoenergetic coating* [18]. THV pellets, acquired from 3M, were first weighted and added to a glass vial. The appropriate volume of acetone was then added to the vial and a screw-top lid was secured to reduce evaporation. Due to acetone's high vapor pressure, the seal must be secure. The vial was then immersed into a sonication bath to mix. While the mixing time was a function of the THV concentration, each sample was left in the sonication bath until all of the solid content was fully dissolved.

Previous experiments using THV as a nonothermite thin film oxidizer would first dissolve THV into acetone at a ratio of 0.5 g THV / 1 ml of acetone. The resulting solution had a low viscosity and was coated onto a rigid substrate via a spin coating method. The thin film was applied, permitting the acetone solvent to fully evaporate. This process ultimately left a uniform THV film behind. The low viscosity was significantly less than traditional 3D printed materials. By increasing the concentration of THV in the solution, we hoped that the solution would increase viscosity.

Initial 3D printing experimentation using this low concentration of THV in acetone proved to be promising. Figure 14 shows THV segmented spread on a glass slide by hand using a pipette. The concentrate of THV of 4.0 g/ml could be relatedly printed without

spreading of the THV outside the original deposition site. The material was dispensed by hand into lines of varying height. Each line readily held its form and adhered to the bed.
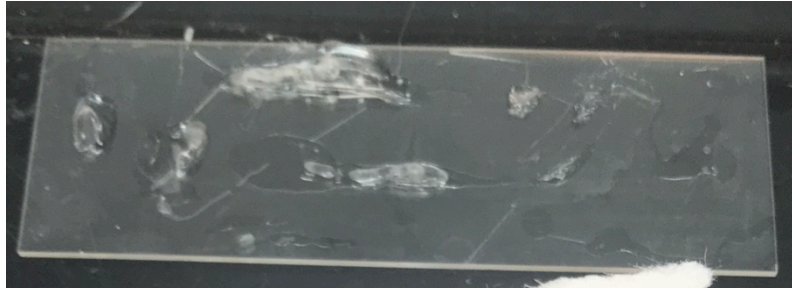
Figure 14 – Prelimary THV printing tests at 4.0 g/ml. The material was dispensed by hand onto a glass slide. The buildplate contains multiple shapes, and lines of varying height.

After several minutes, however, the larger lines began to contract and lose some of their original height. Although unexpected at first, the evaporated acetone had a moderate impact on the THV film after printing. Following Table 2 to create the desired concentration of THV to acetone, sonication of the material for 6-8 hours is required to achieve uniform solution.

The viscosity of each THV concentration was then tested for viscosity using a falling ball viscometer technique. The greater the viscosity of the solution, the more the fluid resists flow. The less flow after print deposition, the greater the geometric tolerances are to the final product. This viscometer device can be seen in Figure 15.

Figure 15 – Viscometer setup consisting of a vertical test tube with marked start and stop lines. The time required for the ball to drop from the top to the bottom of the test tube is monitored by timeplapse photography and used to determine the viscosity of the working fluid.

This viscomenter consists of a tall vertical tube with two sets of red lines marked around its perimeter. A ball of known mass and size is placed into the beaker filled with the liquid to be tested. The ball is then dropped from the top starting line and allowed to drop to the lower set of lines. The process is timed and the time, t, is then recorded for the ball to reach the second set of red lines. This time in minutes is then inputted into the viscosity equation [1]

$$\mu = kt(\rho_f - \rho) \qquad [1]$$

This equation correlates the ball size coefient k, the dencity of the fluid ρ_f, and dencity of the ball ρ to the viscosity in centipoise (cp) of the tested liquid, μ. Table 2 contains the data from this equation as well as the concentraion of THV and acetone in each sample.

Table 2 – Viscosity and Conentration Data

Concentration (g/ml)	0	3	3.5	4	4.5
THV (g)	0	4.5	5.25	6	6.75
Acetone (mL)	1.5	1.5	1.5	1.5	1.5
Viscosity (cp)	0.316	403.95	987.20	1581.29	3907.69
Color	N/A	Blue	Red	Yellow	Green

While testing the various THV solutions, each concentration was assigned a unique color code imparted by the use of food coloring. Only a single drop of dye is needed for each sample. Figure 16 demonstrates the difference in color after completing the sonication bath.

Figure 16 – Homogeneous THV solutions with food coloring.

After a uniform THV/acetone solution was obtained, the resulting material may be cast or print. When dispensed onto a substrate, the acetone quickly evaporated, leaving the THV polymer behind. The concentration of THV and scale of the print (surface are to volume ratio) will determine the time required to evaporate the solvent fully from the deposited THV. Based on initial experimentation, the time required for the THV to fully evaporate is on the order of 130 seconds for a THV box cast with dimensions of 5 mm x 5mm x 1mm. Because of the

mass lost from solvent evaporation, the reduction in volume in the deposited THV may cause greater warping forces than experienced with conventional FDM methods and materials.

To explore the effect of evaporation on the formation of THV layering, a single line of hand-dispersed THV solution was placed onto a glass slide. After waiting 15 seconds for evaporation, another line was dispensed above the latter. Ultimately, Figure 17 demonstrates that 6 layers were dispensed with good adhesion and comformality between layers.
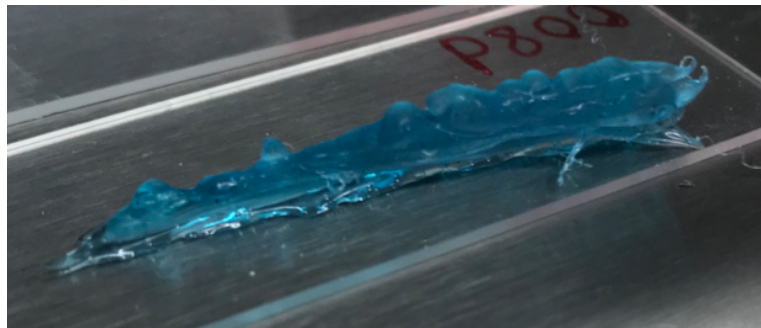
Figure 17 – Hand dispersed THV layer test. The material structurally bonded to each new layer, but showed warping on the right side of the mass.

Although the hand-dispensed sample did not create uniform lines (as observed by the peaks and valleys in the sample), the solution readily bonded to itself (layer-upon-layer) and did not flow over the prior layer. Each layer held its own form throughout the trial and ultimately created a structurally rigid and monolithic entity. The greatest weakness in the material was the volumetric constriction caused from evaporation of acetone from the deposited layers. As each layer was placed, the right side of the material began to curl very slightly. The more material was placed, the greater the warping effect became. In hindsight, the act of extruding each layer from the left to the right may have distorted the adhesion of the first layer to the glass slide. By pipetting the material by hand, it is very possible that we pulled away from the glass slide prematurely, a human error that will not be seen by the

ultimate use of a printer later in experimentation. The printer will have a constant height throughout the dispensing of an individual layer. Thus, any internal stresses had a structural weakness to exploit. Nevertheless, the evaporation of acetone from the deposited layers generated too much shrinkage to sustain 100% adhesion at a 15 second delay between layers.

To counteract the adhesion stresses, two methods were explored. The first was increasing the time interval between each layer. This would allow acetone from a layer to fully evaporate before the next layer and hopefully harden the previous layer enough to counteract internal forces. While in the process of printing, however, one does not have precise control of the time interval between each layer. Large prints naturally have an extended time between passes due to the area the printer needs to cover, but the smaller prints do not have this advantage. A delay would be needed in the modeling software to account for the drying time. G Code (RS-274) is a group of programing languages that controls 3D Printers and CNC machines. The most accepted variant, found on FANUC and similarly designed machines, designate the code G04 P###, the dwell command where the pound signs after the P is the dwell time in milliseconds, as the best method to pause machines mid action [19]. For CNC machines, this can be a simple addition to a premade G Code file, but for 3D Printing, this is a much more difficult task. Printers run the desired model through a program called a slicer, where the model is primed for printing. Each desired model is broken up into layers and then transcribed into G Code. These programs themselves do not have options to add in a dwell command after every layer. Depending on the printer brand, some slicers save the code on an external memory device before being sent to the printer, making this the perfect time to update the code with the desired commands. Others on the other hand, send the

code directly to the printer uninterrupted. Because of the wide variety of slicer programs, this method is not reliable in every circumstance.

The other method is to use a build surface that stimulates adhesion. As Ed Tyson states in his article, *3D Prints warping or Curling? Why it Happens and How to Prevent it,* build plate adhesion is the "likely most important step that you can take to eliminate warping" [20]. Tyson specifically highlights the smoothness of glass and aluminum, the two materials used as build plates in this paper, as major contributors to warping. He highlights the use of painters' tape, glue sticks, or hairspray as the most common methods to roughen up the surface. Due to these methods introducing additional substances into the processing of nanothermites, it was decided to test increase the surface adhesion by negating the smoothness of an assortment of glass slides with different sandpaper grits. The tested slides are in Figure 18.
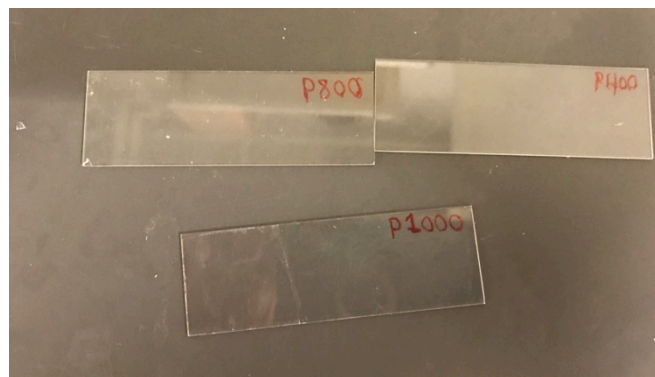
Figure 18 – Three roughened glass slides roughened with (top left) P800 grit, (top right) P400 grit, and (bottom) P1000 grit.

Through the use of the line experiment, it was decided that the P400 grit was sufficient to prevent the warping of 6 layers of the THV/acetone solution. Both finer sand paper grits of P800 and the P1000 displayed the same minor warping present in the original experiment with

a smooth slide. Thus, further experimentation will be using build plates roughened with the P400 grit sandpaper to increase build plate adhesion.

2.2. Graphene Oxide Aerogel

To explore the feasibility of printing graphene oxide (GO) aerogel material for printing, the same hand dispersed line experiments as THV were used. Note that unlike the THV process, two distinct material layers must be deposited to complete a single layer. First, a single line was dispensed of the GO solution, and then 2-3 drops of the EDA was placed into the center of the deposited area. The GO is visibly altered by the introduction of EDA as the gelling process initiates. The color changes from a dark brown to a solid black gel. In Figure 19, large (hand dispensed) gelled samples were formed.

Figure 19 – Photograph of hand-dispursed GO and EDA to create a GO aerogel. The top formation represents a circular dot test. The bottom formation represents an attempt to create a linear assembly.

By the time the solution fully gelled, the thin GO quickly settled into a large agglomeration. GO, being a solution with a very low viscosity, needed the EDA to solidify and prevent further flow. Any time delay between depositing the GO solution and EDA greatly diminished the geometric control of the material. Just like the THV samples, these GO samples have ridges and valleys in their centers. This is due to high concentrations of EDA located where each droplet of EDA was introduced. This may cause problems to the overall structure of the aerogel if printed. To combat this, we dispensed different volumes of EDA on a glass slide first, before placing GO. We hypothesized a pre-deposited and uniform EDA layer would facilitate an even gelation of GO without affecting the adhesion of the material to the bed. If too much EDA is dispersed before the GO, we hypothesize that the GO will gel floating above the plate and will not adhere correctly. Figure 20 highlights the effects of the EDA to the final shape of the gel.
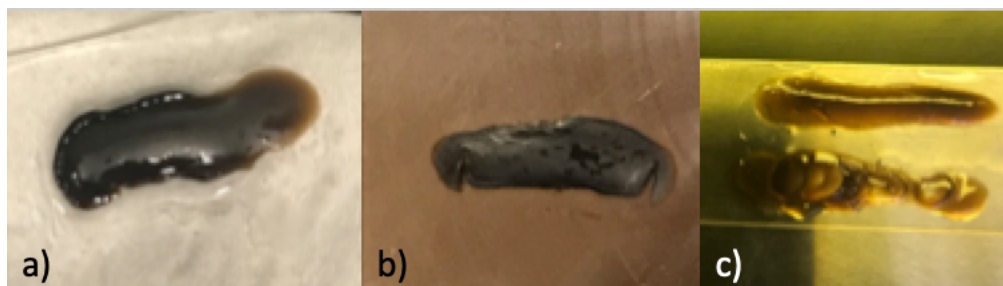
Figure 20 – Initial Single Layer GO Geometry. (a) is a sinlge drop of EDA before the GO, (b) is 2 drops of EDA, (c top) 3 drops of EDA (c bottom) 3 drops of EDA after the GO. The bubbles within this sample are due to the large concentrations of EDA.

A single droplet of EDA proved to be an insufficient volume to support the gelation of a GO line having a length of approximately 1". Dispersing the GO from left to right in the

figure, the GO deposited atop the EDA layer did not fully gel. Although the GO gelled, the beginning of the line (a in Figure 20) absorbed most of the EDA before the end of the GO line completed deposition. This is characterized by the major change of coloring between the left and right sides of the left picture. The gelled GO did prove to be smaller than the GO deposited to a dry glass slide and adhered very well to the plate, addressing a key concern for its printability. When the droplets of EDA increased to two drops in b) and three drops in c), the GO did gel and show signs of increased geometric stability, but not perfectly. For example, the three EDA drop line in top line of c) proved to be the most uniform of the three tests. There was very little in the form of overflow or odd bulges in this test. The line below c) is to have a visual comparison between GO that is dispersed onto a dry glass slide (bottom) and the GO that is dispersed onto 3 drops of EDA. Both used the same amount of EDA. Moving forward, 3 drops of EDA will be used in gelation due to its increased stability.
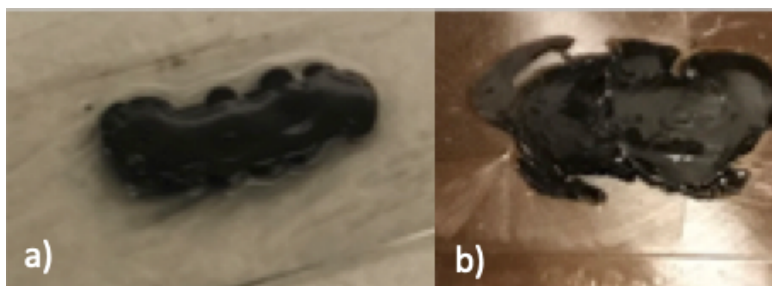
Figure 21 – Initial two layer GO geometry. (a) 2ⁿᵈ layer of EDA and GO. (b) Only 2ⁿᵈ layer of GO.

Next, the GO's ability to build vertical layers was examined. In each test, each layer was dispensed by hand. Figure 21 highlights two variations in this experiment. The two-layer GO aerogel in a) was formed by repeating the same procedure for each layer. The procedure consisted of first dispensing 3 drops of EDA, followed by a layer of GO directly atop the EDA layer. b) used a different technique for the two layers. The first layer was formed in the

same manner as the previous example. However, the second layer skipped the second EDA

deposition. The second layer of GO was directly dispensed onto the previously gelled first

layer. In both techniques, the second GO layer did not adhere to the first layer and quickly

flowed off the already gelled material. The 2nd layer of EDA in a) did retain to the second GO

layer from fully flowing away from the top layer. Although successful in keeping the general

shape of the layer below, neither technique successfully created distinct and adhered layers,

and thus does not pass the layering criteria.

Premixing of the GO solution and EDA was then attempted to avert the gelation time

on the print bed. It was hypothesized that the material could be more easily controlled in a

singular gelled state compared to its two distinct material inks. When creating the mixture, a

GO solution of approximately 0.25 ml was placed into a syringe, and a single drop of EDA

was introduced. A single drop was decided to be sufficient for the small volume of THV.

Figure 22 shows the mixture within the syringe and the outcome of an attempted print using

nozzle diameter of 0.7 mm.
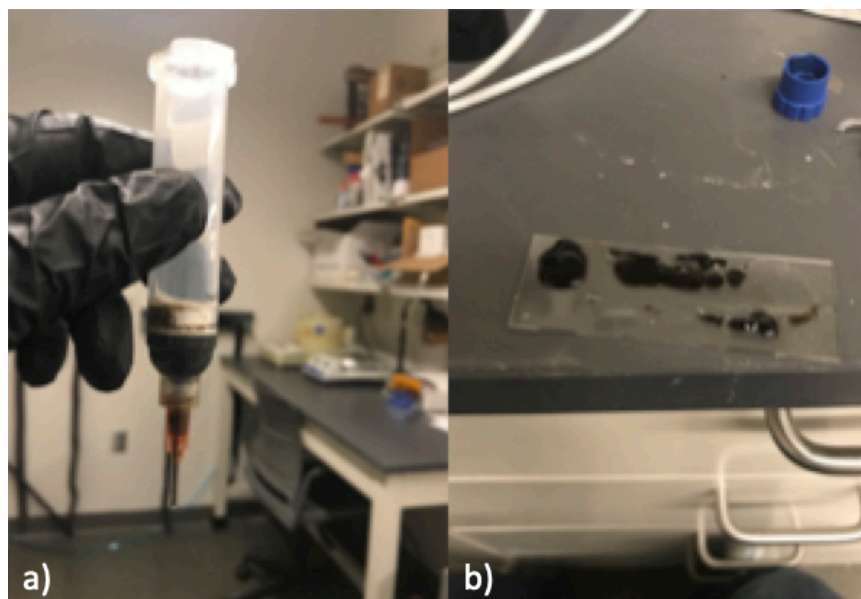
Figure 22 – (a) Pre-gelled GO in a syringe(b) Dispersed GO.

Unlike the previous GO experiments; a uniform material composition was not dispersed through the nozzle when using the pre-gelled GO. Instead, the mixture came out of the nozzle in heterogeneous sized agglomerations. We believe that the inconsistent printing was results of the internal structure of the gelled GO itself. When gelled, the GO layers bond together as discussed in the GO introduction. To break this structure for extrusion through the nozzle, extra force had to be applied. The resulting pressure required to push non-homogeneous GO aerogel through the nozzle was periodically increased. Thus, this method of preparation failed the certification for printing consistently.

To conclude the individual material testing, GO will need future work to uncover a solution to the lack of bonding when printing multiple layers. This may be by the improvement of its physical bonding through binders, the printing inside of a gel well, or a novel answer. Until then, we moved forward and secured a printer to develop the physical printing method of THV.

Chapter 3. – 3D Printing of Energetic-Relevant Materials

3.1. 3D Printer

To achieve scalability, a candidate 3D printing device must disperse the printed materials in a clean and precise manor. Because the material sets of interest are solvent-based, this printer would ideally be self-contained, pneumatic, and have the capacity to disperse a multitude of materials (active thermite materials including support, fuel, and oxidizer) in the same print cycle. Excessive heat generation and minimal shock generation must also be considered as extra constraints to the system because of the combustibility of the printed materials. To achieve this, a drop-on-demand FDM-like method was chosen as the best method to print. This method allows for the clean printing of a material in a manner that can be easily observed while printing. Moreover, there are no extra binders or curable material introduced into the printed solution. To be useful for further research, the material properties after printing must stay similar to those of original source material. Thus, this method relies heavily on the properties of the printed material to bind to itself and no outside sources.

In this work, a Life Science's Biobot Basic was selected as the main 3D printing device. This type of printer is used extensively in the biomedical field as a novel way to print organic matter without the reliance on heat or shock to print the material. Capable of pneumatically printing with 5 different 10cc syringes housed in a single rotating turret, this device is capable to print single part materials like THV or multi part materials like GO. Unlike its contemporaries that use the Cartesian coordinate system, the Biobot Basic unitizes cylindrical coordinates to dispense its material. This is achieved by rotating a circular bed

while coordinating with an X and a Z-axis. The X-axis moves the bed forward and backwards while the Z-axis raises and lowers the turret assembly. Each axis is controlled by lead screws.
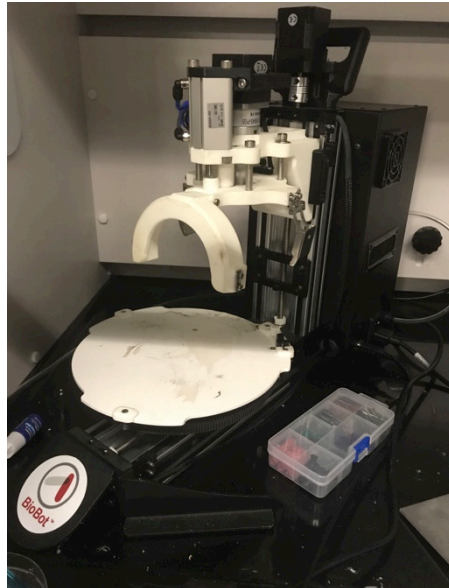
Figure 23 – Photograph of the Biobot Basic.

3.1.1. Initial Setup

Since the Biobot Basic utilizes pneumatic pressure to print, it must be supplied with a pressure line rated between 60 and 100 psi. An external air compressor supplied this pressure. The printer must be connected to a Windows computer with TSIM software to function. This software must be running at all times to control the printer. All control of the printer is directed from this software, so if there is any interruption between the two, the printer will not be able to continue the print. This configuration is termed tethering the printer to the computer. Once connected to a pressure supply and the computer, the printer can be turned on by turning the switch next to the pressure input to the on position.

3.1.2. Print Stages

Figure 24 – Biobot Basic Print Stages

The printer is packaged with three different stages that align different print apparatuses to the desired locations in TSIM. These stages accept slides, petri dishes, and gel wells. Each plate is composed of a painted aluminum sheet with three notches around the perimeter, each correlating to three plastic risers on the main print apparatus on the Biobot. The desired stage simply snaps into place from above.

3.1.3. Turret

The Biobot Basic has a singular turret that holds up to five different 10cc pneumatic syringes in 5 different cells. Each numbered cell contains a single spring that keeps the unused syringes protected in the turret and away from the print. Also, there is a single magnet in between the third and fourth cell. When in use, this magnet is used to initialize the turret and make sure that the correct syringe is in place to print.
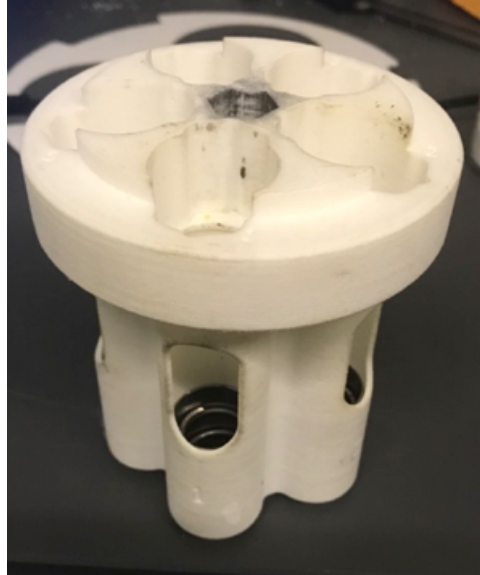
Figure 25 – Biobot Turret unloaded from the Biobot.

To load and unload the turret, there are two metal clips that hold a turret guide (Figure 27) in position. To undo the clips, hold the turret in one hand and pull the clip down and away from the printer. The turret guide should fall away once both clips are unfastened.
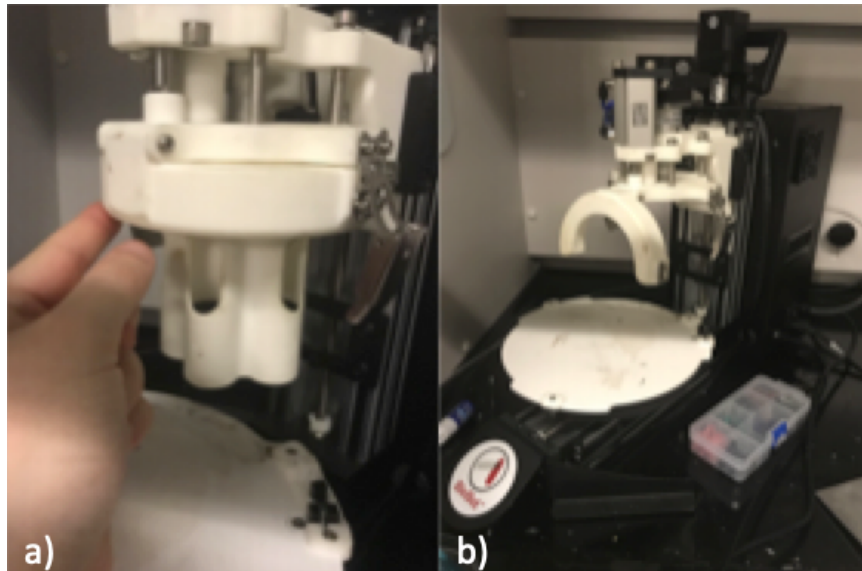
Figure 26 - Unloading the turrt from the printer. Shown are two metal clips (a) that hold up the turret guide (b). When unsecured, the turret is free to slide down and away from the printer.

The turret has a hexagonal notch in the center. When removing or attaching the turret to the printer, this is first the connection point. The notch slides into a hexagonal key shown in Figure 27, and then the turret guide is raised and locked into place. Once set, the turret guide can be raised and secured into place.

Figure 27 – Attaching the turret to the hexigonal key below the printer head. Once the turret is flush with the printer, the turret guide can be raised and secured using two metal clips.

3.2. TSIM Modeling Software

The following section discusses the standard use of the TSIM modeling software and includes our insight and experiences. The sequence execution and options will be presented as a bulleted list for brevity. Any further questions or topics not covered in this section can be answered in the TSIM manual distributed by Advanced Solutions. Upon opening TSIM, we

are greeted with Figure 28. This screen is the primary solid modeling screen for the software. On the top of the window, a ribbon of tabs labeled file, solid modeling, materials, Bioassembly, basic, help, and about can be viewed. Each one coincided with major options and will be covered below.
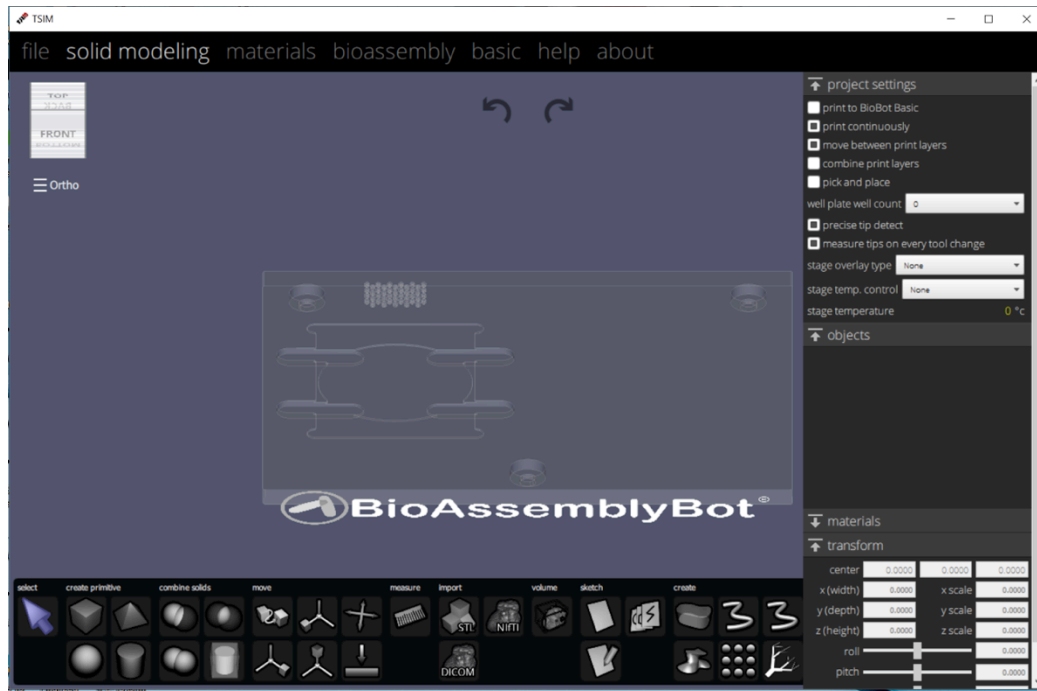
Figure 28 – TSIM initial screen and options.

3.2.1. File

Figure 29 – File Menu

Before discussing the main pages of TSIM, a few things must be said about the file

tab. First, Figure 29 is the tab for the save, open, and export commands. But unlike some

slicers and 3D modeling software, TSIM saves the specific project and material settings to the

saved file. TSIM does not have a global project setting or material settings, so these settings

will not carry over into new projects. Thus, it is important to have a backup of any important

settings in case they need to be reviewed or be used in a new file. Moreover, the only way to

copy a model from one instance of TSIM to another is through exporting it as an .STL file.

The file can then be opened at its destination by using the import .STL tool in the Solid

Modeling tab. Finally; the Biobot Basic will only recognize a single window of TSIM. To

minimize confusion, it is recommended to work in a single window of TSIM when possible.

The printer recognizes the first window of TSIM opened. If the Biobot recognizes the

incorrect instance of TSIM, either all progress in the current window must be transferred to

the Biobot window, or all windows of the software must be closed and the printer reconnected

for it to acknowledge the correct window.

3.2.2. Solid Modeling Menu

The Solid Modeling Menu is the focal area of TSIM. This menu page is where 3D models may be created, imported, or exported from the software. The right strip contains all of the overall options for the project (discussed below). To save confusion later, it is recommended that these options be chosen before designing the model or updating material settings. It is recommended to check the Print to Biobot', 'Print Continuously', 'Combine Print Layers', and 'Choose the Desired Stage Overlay'. Settings not used in the Biobot Basic include 'Precise Tip Detect', 'Well Plate Well Count', 'Stage Temp Control', and 'Stage Temperature'. These settings can be disregarded in normal use of the Biobot Basic. Below is a quick description of each option.

- Print to Biobot - Changes the code and the modeling space to Biobot Basic. The coordinates for printing will be Polar.

- Print Continuously – Simplifies each Z layer to be printed in one continuous line. If unchecked, the Biobot will print each layer in a discontinuous manor. If a line needs to cross another, the printer will stop printing, move its nozzle up, and place it in the desired location. By having this checked, the prints will save time by printing each layer in a continuous manor. Turn on to save time.

- Move Between Print layers – Just added in the newest update. Few tests show that this creates a seamless transition between print layers. If turned on, the printer will fully pick up the nozzle before setting it on the next layer or model. Recommended to be turned off.

- Combine Print Layers – Forces the program to print a layer of each model before moving onto the next layer. If turned off, each model will be fully

printed before moving to the next model. We recommend this to be turned on
so that each layer has time to settle and evaporate before another layer is
dispersed.

- Stage Overlay - Creates a shadow of where the stage will be placed in the
model space. The choices are between printing straight to the bed, onto slides,
onto Petri dishes, or onto a well. Choosing the correct stage overlay simplifies
the process of locating models on the stage and predicting where those models
will be printed.

- Measure tips on every tool change – Each print begins by calibrating the height
of the first nozzle. If checked, this calibration command will be completed at
each instance of a tool change. Increases the accuracy of the printer, but each
calibration introduces a new point of failure and increases print time.

- Well plate well count – States the number of wells used in a well plate. Those
wells are then shown in the virtual build plate.

- Stage temp control – BioAssemblyBot specific setting. Ability to turn on a
heated/cooled bed.

- Stage temperature – BioAssemblyBot specific setting. Controls the specific
temperature of the bed.
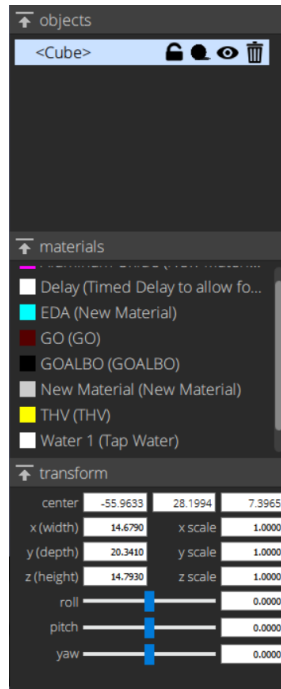
Figure 30 – TSIM Model Settings

Once setup, the rest of the ribbon is used in conjunction with any models created. Objects are where each model can be selected individually. The name of these models can be updated with a single click on the name. After the name, there are four tools. Discussed from left to, the 'Lock' command locks the dimensions and position of the part itself. The 'Roll' command turns the selected model transparent. The 'Visibility' command, (the button that looks like an eye) toggles the visibility of the part. If it is desired to delete the model, the 'Delete" command (trashcan) is the only way to fully erase the model. Backspace does not delete the models. Underneath the Objects section is a section dedicated to the selection of materials. Each model must have a material set to it. To set a material, first select the desired model using the selection tool. Then click on the desired material from this dropdown. The model will change to the color of the selected material.

To create new material parameters or to update existing parameters, click on the Material Tab and visit Section 3.2.3 below.

For building models, everything will input onto the virtual build plate, shown in the center of Figure 30. The bullet points below will highlight a few of the most used tools.
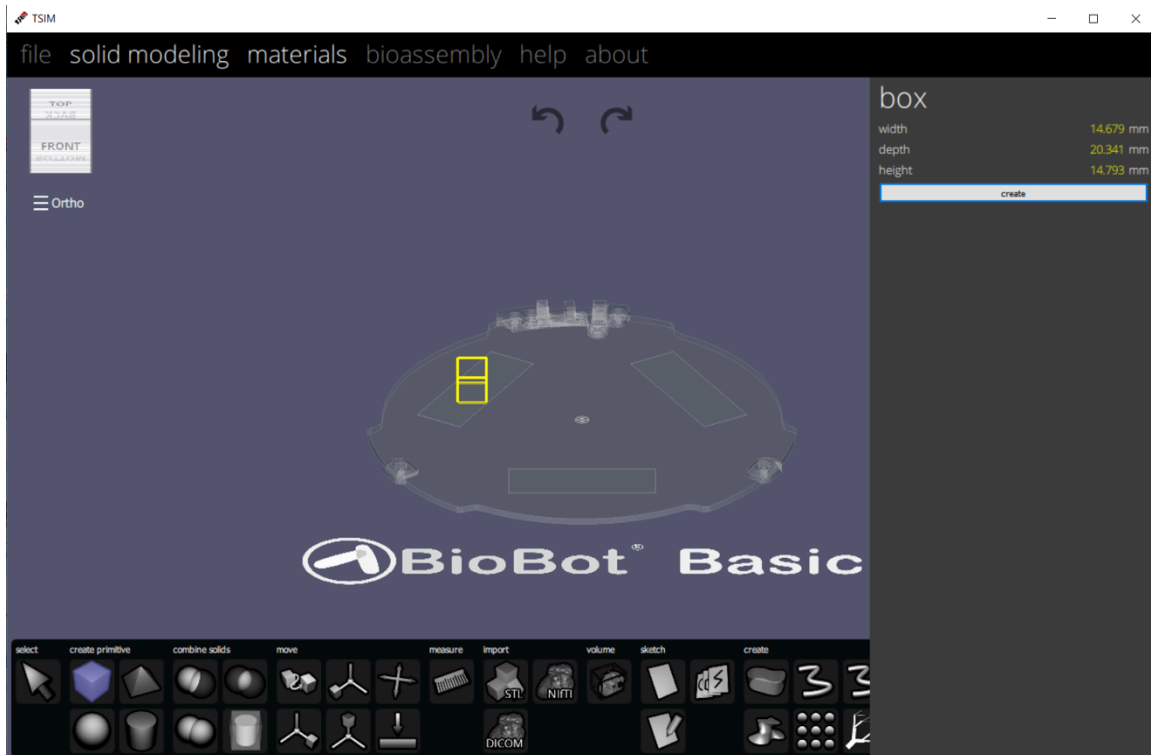
Figure 31 – TSIM Box Creation

- Select – selects any object on the bed. Must be chosen to interact with any models on the build plate. When object is selected with this tool, the object will be highlighted in the objects ribbon on the right side and the "interaction widget" (Figure 32) will appear. This can be used to move (outside arrows) rotate (inside rectangles) or scale (middle squares) the model with a single click. Each color coincides with one of the three axis of the model.

40
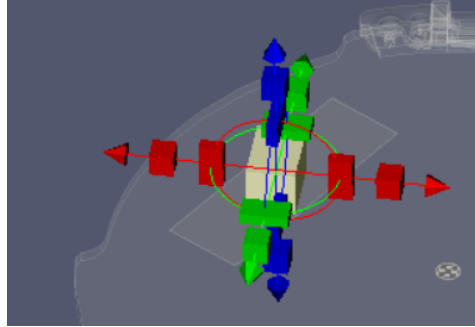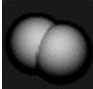
Figure 32 – TSIM Model Movement

- Box – Allows the creation of a single rectangular geometry (Figure 31).

  First click on the build place centers the model; Second click sets the base and

  width, while the third click sets the height. Specific dimensions can also be

  input into the box ledger on the right hand side, but the starting position must

  be chosen with the first click before stating these dimensions.

- Combine Tools – an assortment of tools that allow two separate models to

  interact with each other. Each model must have a section of overlap to be used.

- Combine tool - Simplest way to combine two models into one. The

  printer will treat the combined object as a single model once completed.

- Difference tool - Subtracts one model from the other. This allows for more

  complicated geometries to be made.

- Intersect tool – Important tool for deleting any parts of the models that

  are not overlapped. Keeps the overlapped sections.

41

- Lay Flat – Forces the model to sit on the build plate. Any side can be chosen. Thus the model can automatically rotate so that the selected side is now flush with the build plate. If any models' geometry is updated after creation, it is recommended that this tool is used to replace the model on the build plate. TSIM will not print if the model is floating above or below the build plate.

- Import .STL – Allows for the inclusion of premade .STL files. Opens up a new window where .STL's can be chosen and imported into TIM.

- Sketch – Method to create original geometries through the use of 2D sketches. Sketches can be made on 3 different planes centered on the origin. Each sketch must consist of closed contours. TSIM cannot extrude open sketches. Once created, the Surface and Tube tool can be used to extrude out flat surfaces, or circular tubes.

3.2.3. Materials
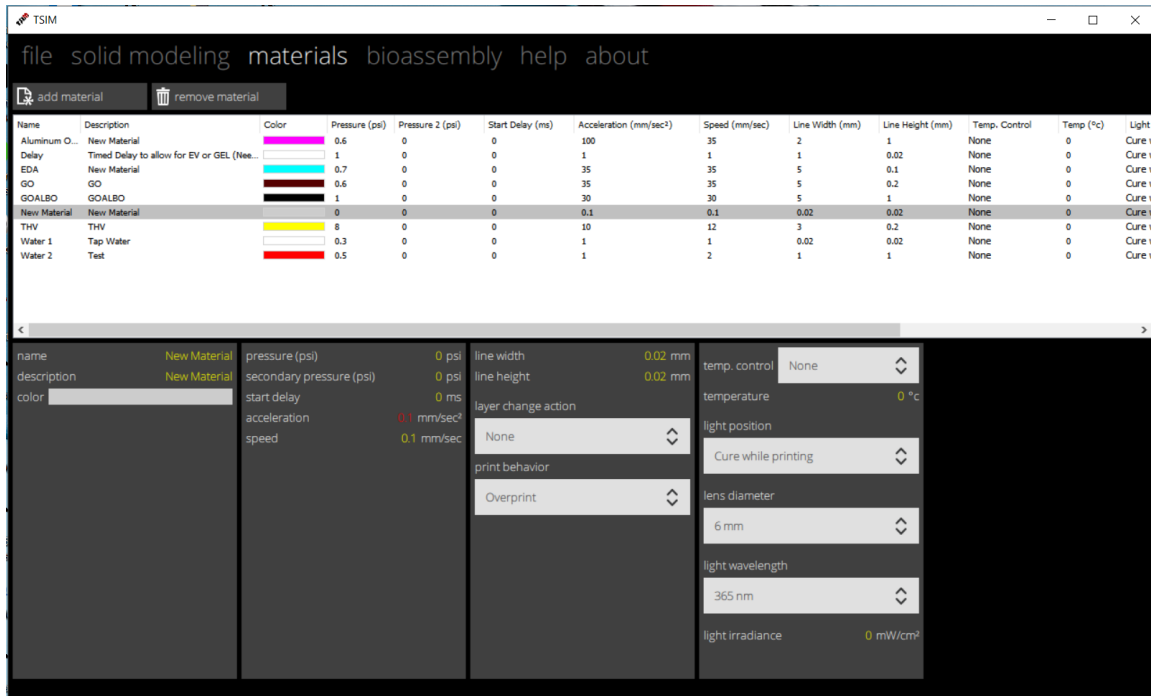
Figure 33 – TSIM Materials Tab.

The Materials tab is dedicated to physical printing parameters. To add materials, click on the Add Material button on the top right. To delete a material, select it in the list below, and then click the Remove Material button. To change the name of the material, select the material in the list, and then single click on the name. Type in the desired name of the material when it is highlighted. The following will be bullet point important settings and descriptions.

- Acceleration (AC) = The acceleration of the nozzle when speeding up or slowing down while printing. This is not a critical parameter. We set this value at 10mm/s and kept it constant throughout experimentation.

- Speed (V_n) - Feed-rate of the nozzle across the print bed in mm/s. Will be discussed further in detail in the Physical Model section.

- Pressure (P) - The gauge pressure (psi) input into the pneumatic syringe. The greater the value, the larger the mass flow rate. The only imperial value in the program. It is very important to note that every other value is in SI.

- Pressure 2 – Backup pressure for the BioAssemblyBot. Not used in the Biobot Basic.

- Start Delay – A delay between the start of the pressure and the beginning of printer movement. Did not explore in this paper, so all values are set to 0. Can be used to calibrate the start of printed lines to be similar to the rest of the flow.

- Line Height (LH) - he height between each layer. The starting layer is decided by the stage line height seen in the BIOBOT Tab the line height.

- Line Width (LW) - The overall line width between each layer. The software can increase or decrease the space between the same layer passes through this value. For testing, was placed at the value 2mm. This large value is known to be too large so that the experimental line width can be accurately measured

- Temp Control – Only used for the BioAssemblyBot. Can turn on and off the heated/cooled build plate.

- Light Position/Irradiance - Only used for the BioAssemblyBot. The bot is equipped with an ambient light tool that can be used to illuminate with light or bathe the print with UV light.

3.2.4. Biobot Tab

This tab is the main tab to prepare and commence a print. The large circle in the middle is a virtual indication of the material to be placed in each cell in the printer turret. If no

materials are shown, the printer is not ready to print. The printer must go through a material

ejection. Click on the button, Load Material to initiate this program. The printer set all of its

moving components to a home position, called a process called 'zeroing', and then the turret

will disengage the pneumatic pump. This button must be pressed before removing the turret.

Once complete, 5 different colors will appear around the large virtual circle. Match the color

of the material with the physical material chosen for that color and place a syringe of material

inside the turret. See section 3.1 for loading and unloading turret. Once complete, click on the

print button to commence printing. A progress bar will appear, and the bot will commence its

initialization and nozzle calibration program.

3.3. Physical Model of the Printing Process

3.3.1. Material Flow Rate

Multiple input parameters must be determined and calibrated to deliver a successful

print. The TSIM material variables must be calibrated against the printer's output parameters.

The parameters optimization may be accomplished, in part, by considering a mass

conservation. Here, the mass flow rate through a circular cross section (syringe nozzle) is set

equal to the mass flow rate of material deposited as an oval on a substrate [21]. The oval cross

section is assumed based on the tendency of viscous prints to flow with respect to gravity. At

steady state, the mass flowing through the nozzle must equal the mass being deposited on the

substrate. Equation 2 associates the speed of the fluid, flow speed through the nozzle, and the

printed material line height

$$\pi R^2 U_N = \frac{\pi R H}{2} U_L \qquad [2]$$

where R is the radius of the nozzle outlet, U_n is the mass – averaged speed through the nozzle, U_L is the mass-averaged speed of the nozzle across the build plate, and H is the line height. Because there is only a single liquid flowing within the flow of the printer, these values are simplified by using the nozzle feed rate across the build plate, V_n for U_n, and the flow rate through nozzle, V_m for U_L. Simplified, the equation becomes.

$$H = \frac{2 R V_n}{V_m} \qquad [3]$$

The use of this equation may be used to predict the appropriate height, H, of the deposited material. If this H is larger than the programmed height, H_T, of the printer, a phenomenon called over-printing will be observed. This occurrence is classified by insufficient contact area of the nozzle to the build plate or too large of a mass flow rate. Signs over over-printing include dragging excess material/whole print, spider webbing, or larger than expected line width/height. On the opposite side of the spectrum, under-printing is seen when H is much smaller than H_T. Considered to be the effect of insufficient contact are of the nozzle or low MFR, under-printing cause smaller than expected line width and height, inconsistency in line width, or failure to print a continuous stream of material at all. These principals are seen in the initial printing tests of 0.5 g/ml THV in Figure 34. This print is designed to be a single layer 2D layer at 5mm x 5mm.
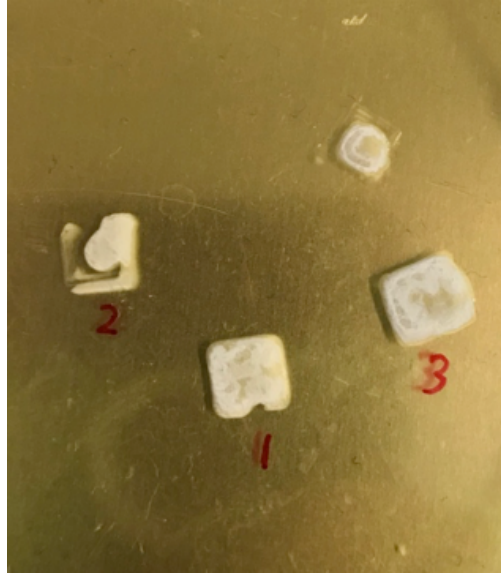
Figure 34 – Initial testing of H for a sample of 0.5 g/ml THV. (1) optimal condtions. (2) Under-extrusion conditions where the material has difficulty extruding at the end of the geometry. (3) Over-extrusion conditons where too much material is extruded ahd the THV begins to overflow on the right edge.

Here, a print of the worst-case scenario concentration of THV (0.5 g/ml) under optimal

printing conditions (1) can be compared to under-extruding (2) and over extruding (3)

conditions. When tuned, the material follows very closely to the desired geometry with no

major holes. But when H is too small, or too large, the desired geometry begins to break

down. Thus, it is vital to understand the correlation between experimental printing parameters

of feed rate V, pressure P, line height, H and the theoretical values of R, V_n, and V_m. This can

be simplified by stating that the feed rate V is the same as the value V_n.

The easiest printing parameter to vary experimentally is the nozzle radius R. The

nozzles suitable for the Biobot 10cc syringes follow the Birmingham Gauge table, as

reproduced in Table 3. Each nozzle can be identified by the color of its base. Radius R is then

calculated by taking half of the inner diameter.

Table 3 – Brimingham Gauge Table [22]

Needle Gauge	Outer Diameter mm	Tol. mm	Inner Diameter mm	Tol. mm	Wall Thickness mm	Tol. mm	Color ISO
20	0.908		0.6		0.152		Yellow
21	0.819		0.51		0.152		Deep green
22	0.718	−0.0064	0.41	−0.019	0.152	±0.0064	Black
23	0.641		0.34		0.152		Deep blue
24	0.568		0.31		0.127		Medium purple

Changing the pressure applied to the end of an extrusion syringe and speed variables in the "Materials" tab in the TSIM software are also readily accessible variables that can alter printing parameters. TSIM's "Speed" variable directly correlates to the nozzle feedrate V_n. The value from TSIM can be directly input into the equation 3. P directly correlates with the TSIM "pressure" setting. By setting the pressure, the combination of the orifice equation, equation 4 paired with the defining equation for mass flow rate, equation 5 [23] may be used to calculate the velocity of the material though the nozzle.

$$Q = A_o C_d \sqrt{\frac{2}{\rho}(P)} \qquad [4]$$

$$Q = \rho A_o V_n \qquad [5]$$

By simplifying the two equations, we see

$$V_n = \frac{C_d \sqrt{\frac{2}{\rho}(P)}}{\rho} \qquad [6]$$

where Q is the mass flow rate of the nozzle in grams per seconds, A_o is the area of the nozzle in meters, C_d is the coefficient of discharge (0.62), and ρ is the density of the material in kilograms per cubic meter. The mass flow rate from these equations can also be compared to

the mass flow rate seen through experimentation. After printing, each print was weighed. This weight was then divided by the averaged print speed of the model. The average was used to mitigate the human error seen by taking measurements with a stopwatch. A comparison will be drawn in the following chapter.

3.3.2. Rheological Characterization

Rheometry, or the study of a material's flow and deformation properties, uses experimental data to measure fluid viscosity. Newtonian fluids are easier to model because their kinetic viscosity is constant at all shear rates. Practically speaking, this is relevant because the viscosity of the fluid is the same in the syringe, when flowing through the nozzle, or on the build plate. For shear-thinning materials, on the other hand, the viscosity of the fluid is directly proportional to the shear stresses exhibited on the material. Shear-thinning is ideal for printing. As ink travels through a printer, the rapidly decreasing diameter of the nozzle enacts large shear stresses on the material. In this state, the shear rate (rate of deformation) exponentially increases. More shear-thinning material can flow into the nozzle at a given force when compared to Newtonian fluids. Once ejected, the material stabilizes its viscosity, reducing its deformation. But if the material is a Newtonian fluid, extra force will need to be applied to counteract the viscous forces, as they do not thin when shear forces are applied.

The most efficient way to identify Newtonian and Non-Newtonian fluids is by examining its shear rate vs. shear stress curve. In Figure 35, the Newtonian fluid is a linear green line while the shear thinning fluid is presented as the exponentially increasing red line.
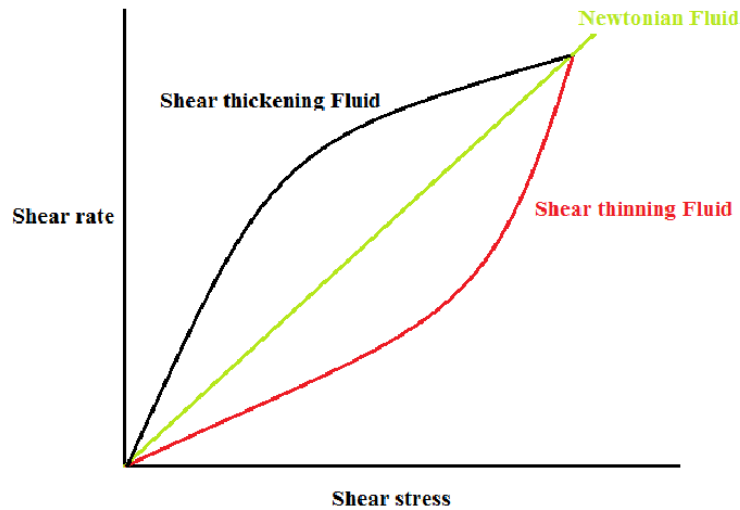
Figure 35 – Shear- thinning and shear-thicnkening fluids compared to Newtonian fluids.[24]

To examine the rheometry of THV and GO, a Brookfield Ametek DV3T rheometer was utilized. The DV3T (Figure 36) is a rotating bobber type viscometer/rheometer that indexes the flow of the tested liquid around the bobber. When rotating, the fluid's torque acting on the rotating bobber is measured by an internal spring. Shear stress and shear rates were tabulated for the Newtonian test along with the viscosities to compare with the Ball Drop.
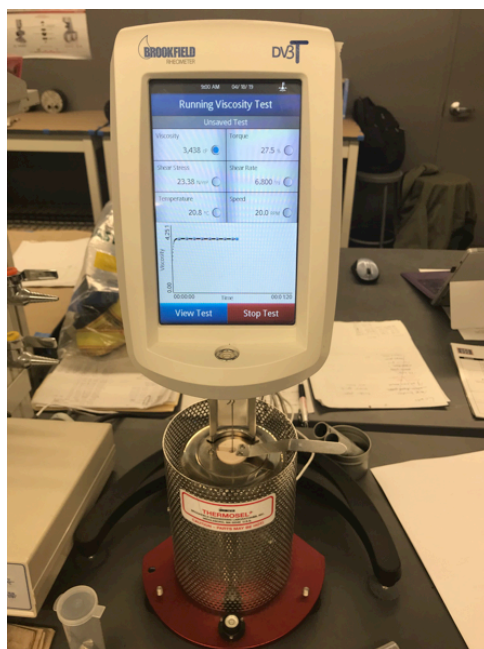
Figure 36 – The Brookfield Ametek DV3T rheometer.

The manual for the DV3T recommends collecting data when the input torque is between 10% and 90% where % is units in dynes/centimeters [25] or Newton-meters. This can be adjusted by increasing the angular velocity of the bobber. When testing in this range, the tolerance is guaranteed to be less than ± 100 cp. There can be large internal errors when working fluids outside of the torque range, specifically the measurement of the internal spring. Temperature was held constant at 23°C throughout testing. Table 4 and Table 5 highlight the results for samples of 4.0 and 4.5 g/ml of acetone. Care was taken to make sure each measurement was in the correct range for % Torque. The averaged viscosities were then compared to the Ball Drop test in Table 6.

Table 4 –Averages DV3T trial values for THV at a concentration of 4.0 g/ml

Axial Velocity (RPM)	15	25	35	50	75	100	Total AVG
Viscosity (cp)	1724	1690	1686	1689	1693	1696	1696.33333
Shear Stress (N/m^2)	8.79	14.37	20.06	28.71	43.17	57.65	28.7916667
Shear Rate	5.1	8.5	11.9	17	25.5	34	17
% Torque	10.3	16.9	23.6	33.8	50.8	67.8	

Table 5 – Averages DV3T trial values for THV at a concentration of 4.5 g/ml

Axial Velocity (RPM)	10	20	30	40	50	60	70	Total AVG
Viscosity (cp)	3416	3434	3394	3370	3329	3303	3267	3359
Shear Stress (N/m^2)	11.62	23.35	34.62	45.84	56.58	67.38	77.76	45.3071429
Shear Rate	3.4	6.8	10.2	13.6	17	20.4	23.8	13.6
% Torque	13.7	27.5	40.7	53.9	66.6	79.3	91.5	

Table 6 – DV3T and Ball Drop Viscosity comparison

Material	GO	4.0 g/ml THV	4.5 g/ml THV
Ball Drop Viscosity (cp)	N/A	1581.29	3907.69
DV3T Viscosity (cp)	15.12*	1696.33	3359

* Maxed out at 7.6% torque at max speed

The GO did not reach the desired 10% minimum % Torque in the DV3T testing. At a maximum of 250 RPM, the averaged viscosity is 15.12. Even if this value is inaccurate, it is only 0.8% of the viscosity of the 4.0 g/ml test. Such a wide separation of the two displays the major flow differences between the two materials. GO readily deforms into a droplet when dispensed, while shear stress has to be applied to the THV to instigate any major flow. Moreover, the GO could not be tested at varying angular velocities. Thus the examination of GO's flow characteristics could not be examined. It is recommended to increase the viscosity of this fluid before looking into this matter.

As for the THV the linearity of Figure 37 denote a Newtonian interaction between the shear stress and shear rate of the fluids. Moving forward, the concentration of 4.5 g/ml of THV was chosen as the tested concentration. Although this material is not ideal for the

printing process due to its Newtonian characteristics, this material will have the best

geometric control. Compared to the other materials, the high viscosity will limit the

deformation after extrusion. We expect that the fluid flow will need a large force to overcome

the viscosity of the fluid.
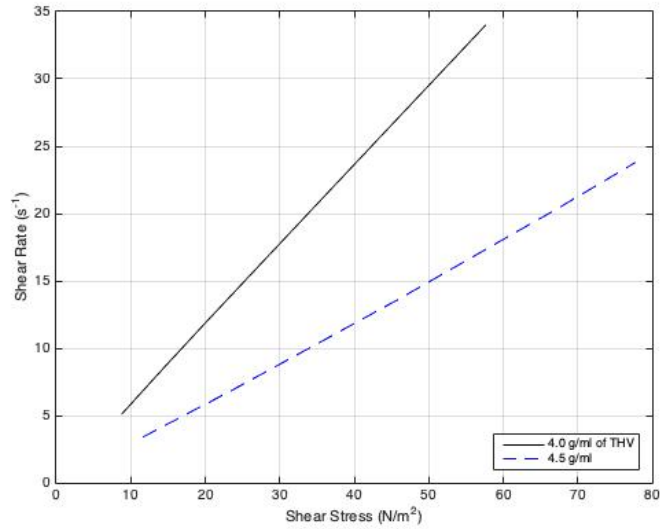
Figure 37 – Experimental DV3T testing for two concentrations of the THV/acetone solution. The THV solution exibits strickly newtonian behavior.

Chapter 4– Experimental Printing Characteristics

When testing the print characteristics of the THV solution, two main experiments were performed. The first test was a model designed to review the individual line characteristics of printed THV lines compared to the input parameters in TSIM control software If successful, the experimental data can be used to predict and calibrate the printer to desired settings. The second test was designed to test the geometric and layering characteristics of the printed.

4.1. Repeatability

Four, 5mm x 5mm x 2mm model boxes were generated using TSIM. The first box is present as a means initiate the flow through the nozzle. If there is an absence of flow, dried material, or any other errors, this box will be a qualitative indication to abort the print. The next 3 boxes (Two trials in Figure 38) are used for the purpose of quantifying print characteristics.

Figure 38 – Example of two separate LH trials. The first trial, seen as the three boxes on the left, have a TSIM LH of 0.4 mm. The next trial for a LH of 0.6 mm. The 0.4 mm test had level lines with very little pooling. The taller 0.6 mm test began to show the signs of under – extrusion, uneven lines, pooling, and expecally in the top model, missing lines.

While printing, a stopwatch was used to time the completion of each model. A quick measurement of the last 3 boxes was performed once the print was complete. A dial calipers was used to measure the largest line width of the print on the bed. Then, the print was taken off the bed, and the height of the print was measured at the tallest point. Finally, the print was placed on a digital balance to find its mass. Mass will then be divided by print time to determine the mass flow rate (MFR). These measurement techniques are shown in Figure 39. The same model file was printed again, first by increasing the pressure, P by 1 psi per iteration. Once completed, the data was then analyzed and plotted in Figure 40. The experimental mass flow rate tapered off at 8 psi, so P was set to this value for future experimentation. The line height, H_T, was then varied by 0.1mm. The goal of this trial was to try to match the printed line height with the line height used in the TSIM software. Finally, the largest V_T will be used in varying the speed. Each of the 3 measured prints per trial was averaged to help negate variability and measurement error.
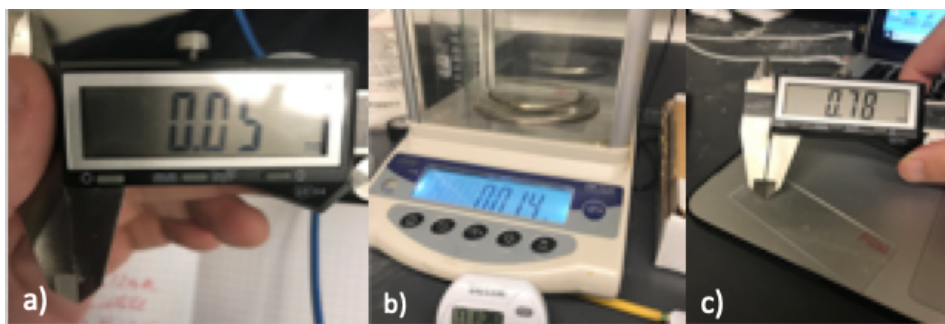
Figure 39 – Exampes of hwo to measure the (a) line width, (b) mass, and (c) line width

The error for these instruments is the minimum accuracy measurement of the device. Each device's accuracy was transcribed in Table 7 below. Future discussions will include a quick discussion on the error of each.

Table 7 – Accuracy of measurment instrumentation

	Dial Caliper	Digital Scale	Stopwatch
Accuracy	±0.01 millimeters	±0.001 grams	±0.1 seconds
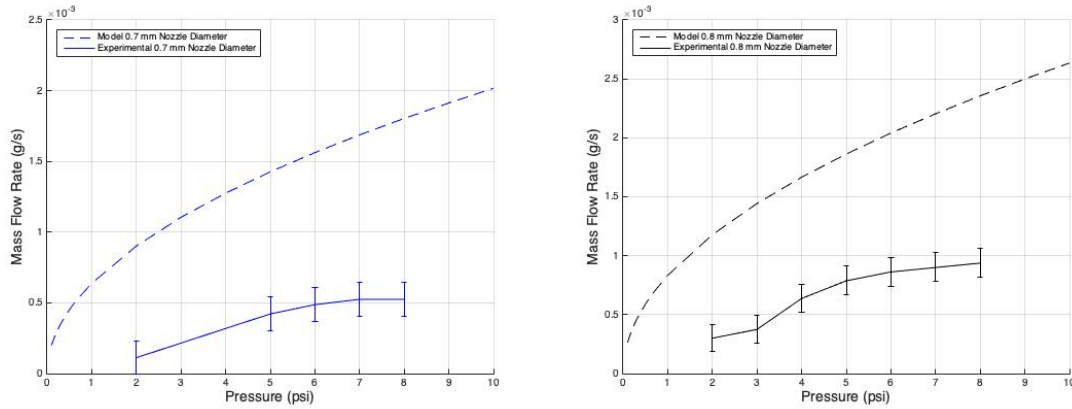
Figure 40 – Theoretical and experimental mass flow rates of 0.7 diameter (left) 0.8 diameter (right) vs input pressure.

The first parameter varied was tested was the pressure applied to the syringe. This is one of the most influential variables in the printing process because it directly influences the MFR. If the printer has a greater mass flow rate, then more material will be dispensed in a given time. The other parameters for this test are constant at LH of 0.2 mm, LW of 2 mm, and speed of 4 mm/s. Line width was theoretical and experimental MFR are plotted in Figure 40 for three different nozzle diameters. The orifice equation, Equation [4] was used to calculate the theoretical mass flow rates of three chosen nozzles, and both experimental and theoretical calculations used the THV concentration of 4.5 g/ml. Moreover, the equation uses the inner diameter of the chosen syringes as well as the coefficient of discharge (C_d) has the standard value of 0.60 for a sharp orifice [26]. The theoretical data has a logarithmic slope that starts the flow after 0 psi. The experimental data, on the other hand, began flow once the threshold pressure of 2 psi was exceeded. This threshold pressure indicates that the static resistance of the THV is not negligible. Because of this discrepancy, the experimental mass flow rates significantly lower than the calculated MFR values. The model (Equation [4]) does not take into account the friction seen within the syringe as well as backpressure in the pneumatic

pump. This friction must be overcome to begin any flow. Moreover, it is to note that when the

accuracy of the instrumentation is included, the error bounds cover only a small area

underneath the model's graph. With an area this small, the choice in instrumentation is sound.

One method to lessen the instrumentation error would be by increasing the run time and

overall size of the print. This test averaged at 8.89 seconds to print at the above settings.

Further testing can push to 30 to 60 seconds to have a better range of values.

Returning to friction forces, if this threshold pressure is included into the orifice

equation by subtracting it from the input pressure, Figure 41 is the result.
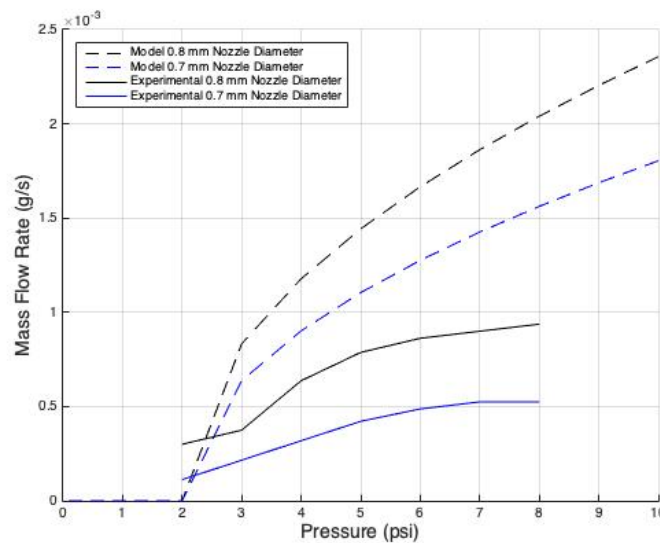
Figure 41 – Updated theoredical and experimental mass flow rates of different nozzle diamters vs input pressure. Subtracted the threshold pressure from the input pressure to model the experimental force needed to overcume friction. The updated model is much closer to the experimental values, but still not perfect. Since mass flow rate scales as the square root of pressure, increasing pressure has a diminishing return in MFR A value of 8 psi was chosen as the optimum value because the sensitivity of MFR to small changes in pressure were marginal.

After initial testing with the purple nozzle (0.55 mm, diameter), this diameter was deemed

inadequate because material readily solidified within the nozzle prior to extrusion on the build

58

plate. Although the smaller diameter nozzle proved to be capable of printing with greater detail and a smaller MFR compared to the other nozzles, the nozzle failed to successfully print in experimentation. An example print with the 0.55 mm diameter nozzle may be observed in Figure 42.
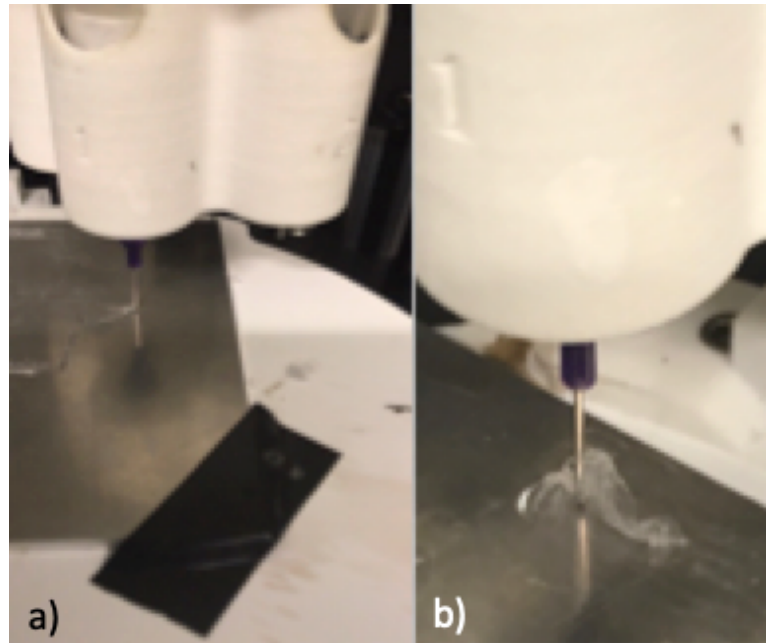
Figure 42 – Printing using the purple (0.55 mm diameter nozzle). Material readiy solidified to the nozzle mid print (right). Prints coninued like this untill this mass pulled up the entire print (right).

At the beginning of the above print, it was evident that there was a buildup forming. As the print continues, the mass began to pull at the lines around it until the whole print was torn off of the plate. We consider this a catastrophic error. The print in Figure 42 b) cannot be salvaged. The same failure was seen at every pressure and line height tested, and thus denotes that this nozzle is unreliable in printing. Experimentation with larger diameter nozzles did not have the buildup seen above.

Pressure also impacted the desired line height and line width to accommodate

variations in mass flow rate. These print parameters are the best indicator of over/under

extrusion. When line height is divided by the line width, a dimensionless area ratio is

formulated. This aspect ratio disregards the overall final shape of the print and focuses on

geometric similarities of the print. For example, when the experimental data is plotted against

the TSIM inputs in Figure 43, most of the values ride below the model.
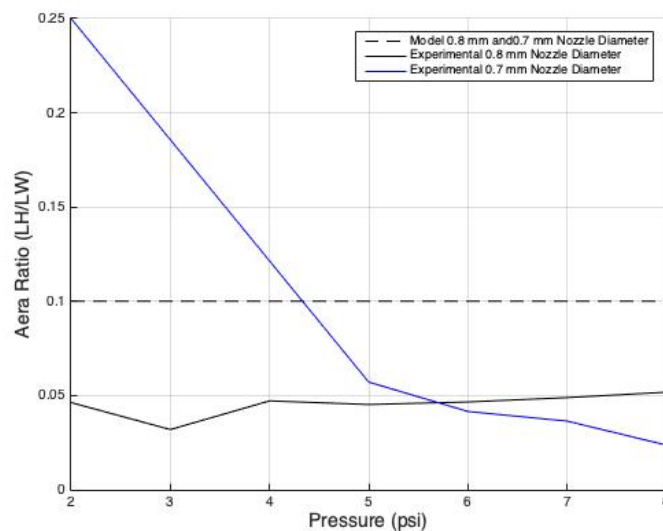
Figure 43 – Aspect ratio of the printed line at differet pressures.

Anything above the modeling line is considered to be printing in an under-extrusion since the

line height is the dominant variable in the ratio. Below the dotted line is considered over-

extrusion. The print is extruding too much material for the given TSIM line width and line

height. The print itself is within this region specifically because the chosen line width of 2mm

was much greater than the desired value and 0.2mm line width is creating a flow constriction.

This constriction is directly leading to a larger line width compared to its line height

Increasing the TSIM line width or decreasing the height will directly lower the dotted model

60

line. Pressure changes do not have any major impact on the aspect ratio. In this way, the

printer can use aspect ratios to calibrate the line width and line height. Because the TSIM LW

variable of 2 mm was designed to be large in the outset, increasing this value further would be

counterintuitive. The TSIM LH should be increased until the experimental ratios approach the

model ratio. Figure 44, a diagram from the *Monoprice Maker Select Manual* verifies the

effect of changing the line height and its effect on line width.
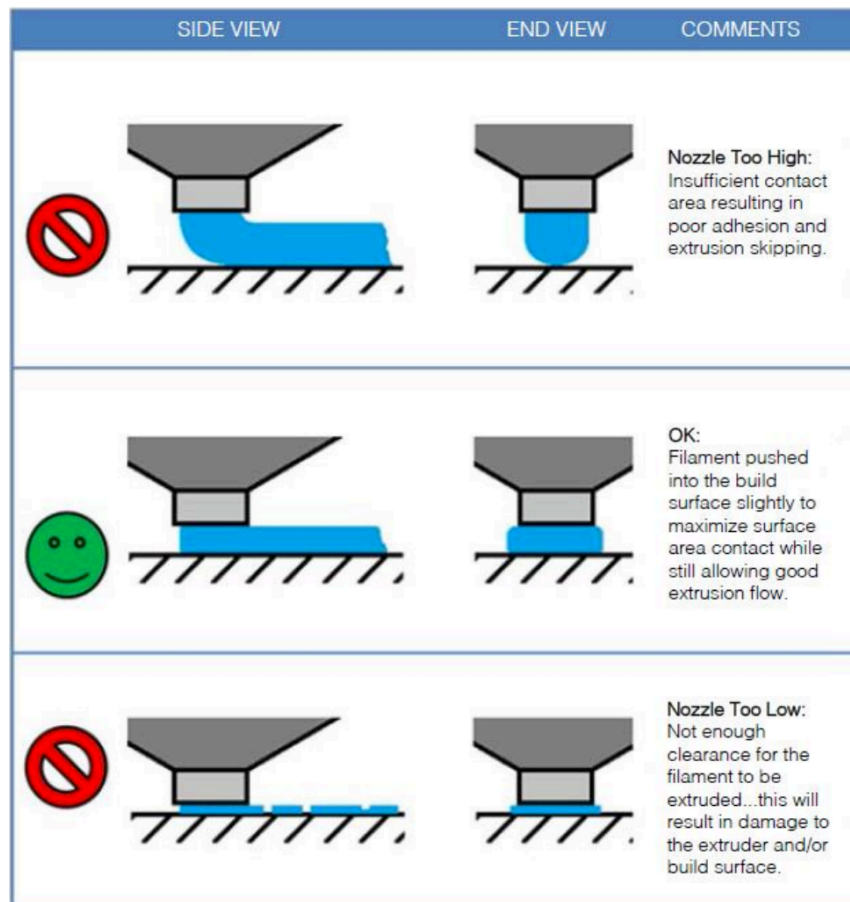

Figure 44 – Nozzle diagram of (top) under-extrusion, (middle) calibrated printing, and over – extrusion (bottom). [27]

In the top image, the line height is too large for the flow of material. Flow is not

restricted at this height, but as the Monoprice Manuel comments, there is still "insufficient

contact" for the printer to print efficiently [27]. Thus, the line width is comparatively narrow, creating a very large aspect ratio. This is certainly would be in the under-extrusion area of Figure 43. Moving on, the central depiction can be considered a fully calibrated print. If graphed, the aspect ratio of the printed LH and LW are considered to be approaching, if not on the dotted model line in Figure 43. When printing, this calibrated print utilizes the settings that allow the nozzle to directly dispense material onto the plate without interfering with the flow exiting the nozzle. If the nozzle did begin to interfere, the nozzle was too close to the bed; the last image described it flawlessly. There was not enough space for the material to fully escape the nozzle, so backpressure began to work against the MFR. Depending how severe the backpressure, the drop in MFR can be noticed by a drop in LH or by an inconsistent wave pattern at the material's edges. Low LH does create a, aspect ratio lower than the model values. This type of printing can be categorized as overprinting.

In Figure 45, the line width is plotted with respects to pressure and nozzle diameter at a constant line height. For a model with the desired line width of 2 mm, the pressure of 8 or 9 would be considered optimal. The pressure at 8 has a line width very close to 2 mm. But if the pressure is increased or decreased, it can be expected that the line width will be affected lineally. If a specific line width is desired for a print, Figure 45 can be used to select the correct pressure and nozzle inner diameter. Note that the larger diameter cannot reach smaller line width, so the smaller, more sensitive 0.7 mm diameter must be used. This logic follows the MFR seen in the smaller 0.7 mm and 0.55 mm nozzle in Figure 41, where the backpressure on the nozzle must be overcome.
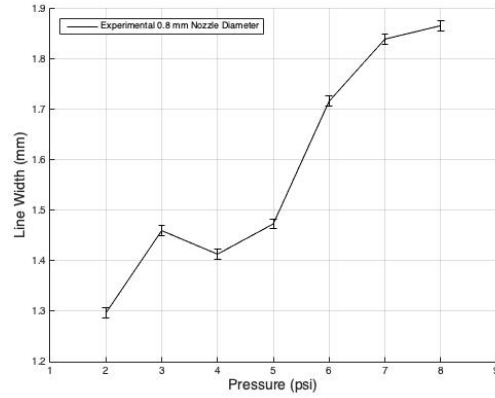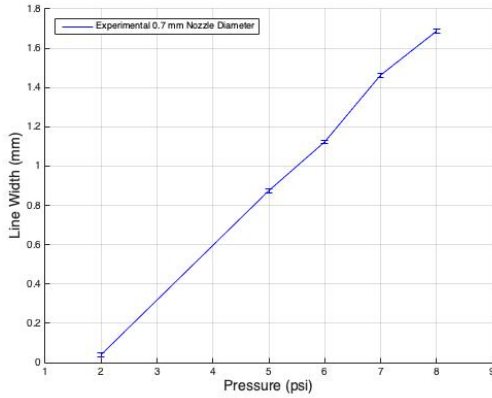
Figure 45 – Line width vs. pneumatic pressure. Test line width was 2 mm, line height was 0.2 mm, and speed was 4 mm/s.

Next, the pressure was compared to the measured and calculated line height. Calculations for the model followed Equation [3], where V_m is 4 mm/s, R is the radius of the inner nozzle, and V_n is calculated from Equation [6] and experimental MFR from Figure 41. Except for the smallest pressure of the 0.7 mm nozzle, the measured line height does not change when the pressure increases. This further proves the classification of over-extrusion for these prints. All of these pressures are above the optimal values for a LH of 0.2 mm and a speed of 4 mm/s. Any local change in pressure does not provide enough nozzle clearance to increase the line height. The only place this may not be the case is for the 2 psi test of the 0.7 mm nozzle. This value begins very close to the expected calculation. With this information, we decided to begin examining the clearance and THV LH of the printer.
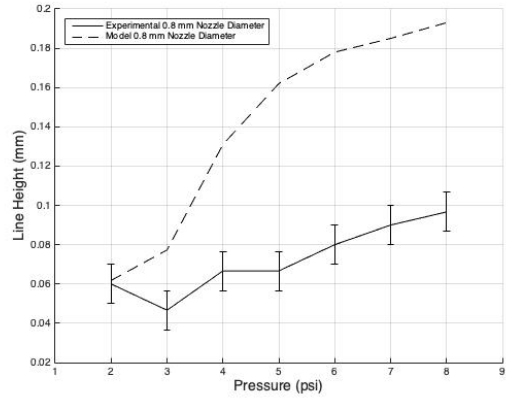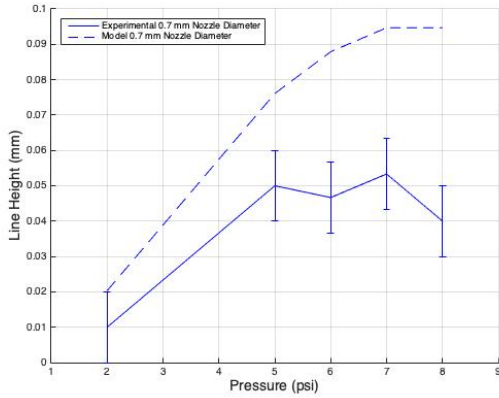
Figure 46 – Measured line height vs. pnumatic pressure.

Next, the line height was varied by 0.1 mm for each trial. The constant TSIM variables for this test were 8 psi pressure, 2 mm line width, and 4 mm/s speed. 8 psi was chosen from the pressure experiments due to its low sensitivity for MFR and the highest difference between the measured line height and pneumatic pressure. Once commenced, the MFR was computed again by dividing the weight of the individual models printed by the time it took to print. Figure 47 is the result.

Figure 47 –Mass flow rate vs. TSIM line height.

This graph is a fantastic numerical description of Figure 44. The tests started at a LH of over-extrusion. As the LH increased, so too did the MFR as the flow restrictions decreased. The MFR then plateaued at a LH of optimum printing, and then began to decrease again when the LH proved to be too tall. The smaller 0.7 mm nozzle perfectly displays this phenomenon, while the larger 0.8 mm nozzle has not fully ente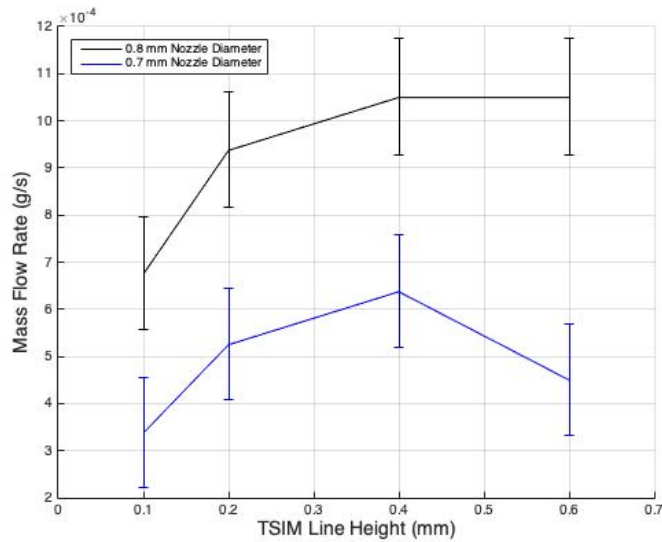red the under-extrusion range. if it had, the MFR would begin to taper off like the smaller nozzle. Through the use of this graph, 0.4 mm stands out as a candidate optimal value for the THV setting.

Before moving to the speed tests, it is important to view the aspect ratios through this experiment. Seen in Figure 48, the aspect ratio starts out near the modeled ratio, but does not have the same slope. The THV LH is directly changing in this experiment, thus it is surprising that the aspect ratio of the experimental data stayed relatively constant. There is an indication of an increasing slope in both of the nozzle tests, but it is important to note that the TSIM LH does not have the same effect as experimental LH on aspect ratio. This may be due to the

rigidity of TSIM's LW. When printed, the material spreads out to its desired LW. This final

LW may correlate to its LH in a way that preserves a repeatable aspect ratio. TSIM does not

have the luxury of adapting its LW to the material. Thus, we have included graphs of the

experimental line height (Figure 49) and experimental line width (Figure 50) below. These

graphs can also be used to predict experimental values and calibrate the printer. Through the

use of these figures, it we concluded to set the TSIM value of LH to be 0.4 mm and LW to be

0.6 mm
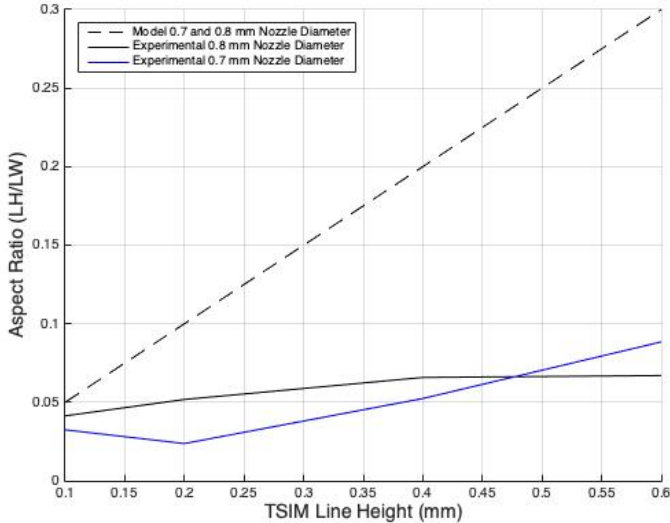
Figure 48 – Aspect Ratio vs. TSIM line height.
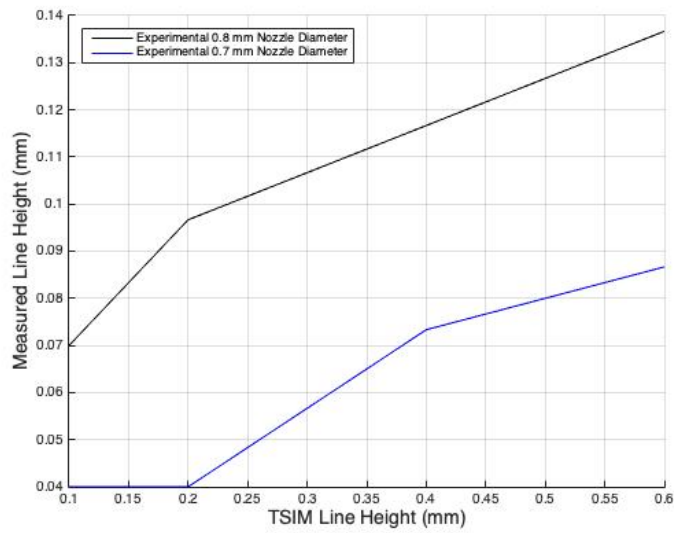
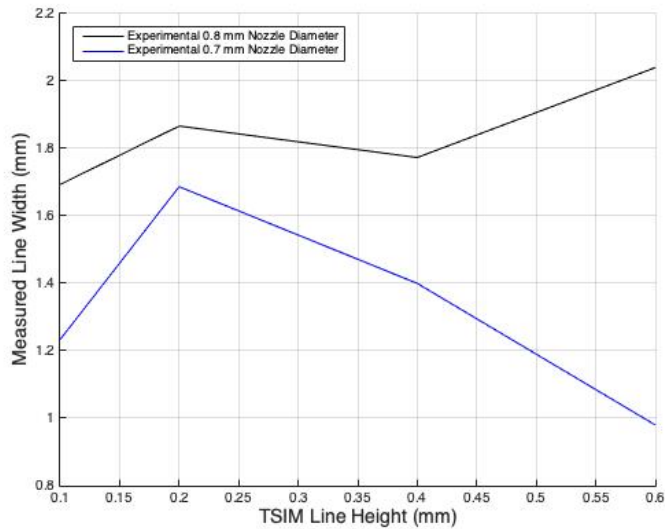**Figure 49 – Measured line height vs. TSIM line height.**

Figure 50 – Measured line width vs. TSIM line height.

Finally, the speed was varied by 2 mm/s per trial. All of the previous optimal values were used in this experiment (Pressure of 8 psi, LH of 0.4 mm, and LW of 0.6 mm). The mass flow rates were then compared to the speed in Figure 51. Each value of MFR used the

corresponding print time to normalize the flow. Increasing the speed variable naturally

decreases the time, so the MFR should be fairly constant. But in Figure 51, the MFR

decreases slightly. For the 0.7 mm nozzle, this slope is contained within the error bounds, so it

is reasonable to assume that the slim decrease is due to the error. Thus, a flat MFR is possible

within the error bounds. As for the larger nozzle, there is a sharper decline in respects to time.

A horizontal MFR does not fit inside of the error bound for this nozzle, so there has to be

some decrease with time. The decreasing MFR may be due to the increased print speed

amplifying timing errors in the start or completion of each model. When moving from model

to model, the flow has to reset. There is a delay between the start of the nozzle's movement

and the flow of the print. If this error becomes a major setback, TSIM has a built in nozzle

delay setting within the Materials tab that allows for a millisecond delay between the start of

the pneumatic pressure and the start of the nozzle movement.
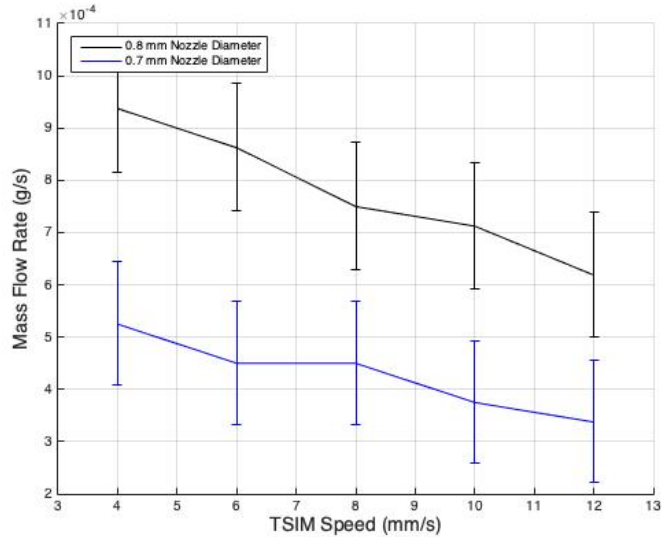
Figure 51 – Mass flow rate vs. TSIM Speed.

Continuing, the aspect ratio should be constant with a change of these values. But, Figure 52 does not verify this claim. There is a single rogue value in the 0.7 mm test, but otherwise, the values slope downwards. This highlights that the line height is most likely getting smaller in respects to line width. This is proven in Figure 53, where there is a major valley at 6 mm/s. Although the LH is trending down as a whole, this peculiar spike does not have the same effect in LW (Figure 54). This is the cause of the odd aspect ratio, a small LH. It is true that both the LW and LH decrease as the print increases speed. Less mass is actually dispensed onto the plate because the print is completed in less time. So, the material that reaches the build plate is less at a specific instant as the TSIM speed value increases. So through the following figures, we decided to choose 10 mm/s as the optimum value. This is due to the softening of the LW for the 0.8 mm nozzle in Figure 54.
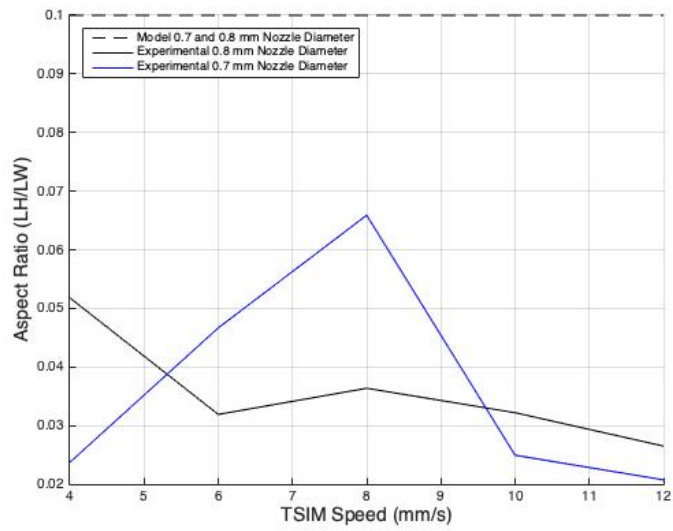
Figure 52 – Aspect ratio vs TSIM Speed.

Figure 53 – Measured line height vs. TSIM speed.
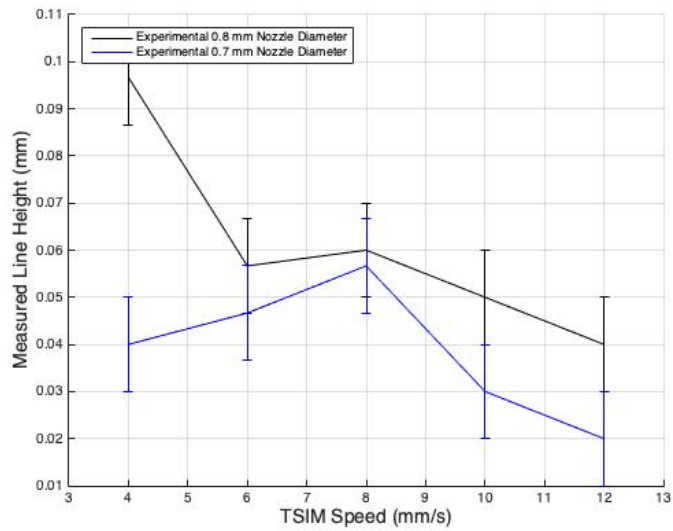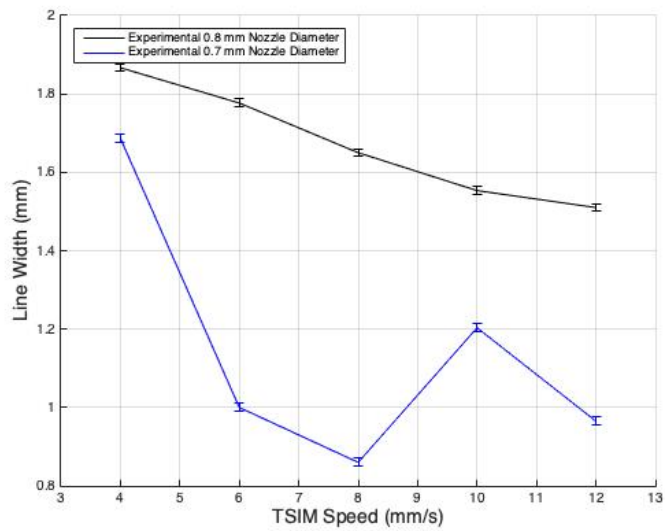
Figure 54 – Measured line width vs. TSIM Speed.

4.2. Control of Geometry and Multiple Layers

Although warping has been examined for single, hand extruded layers of THV, the inclusion of the Biobot as the dispersion technique will need to be examined. Consisting of two main models, the first is a serpentine pattern that follows Figure 55.
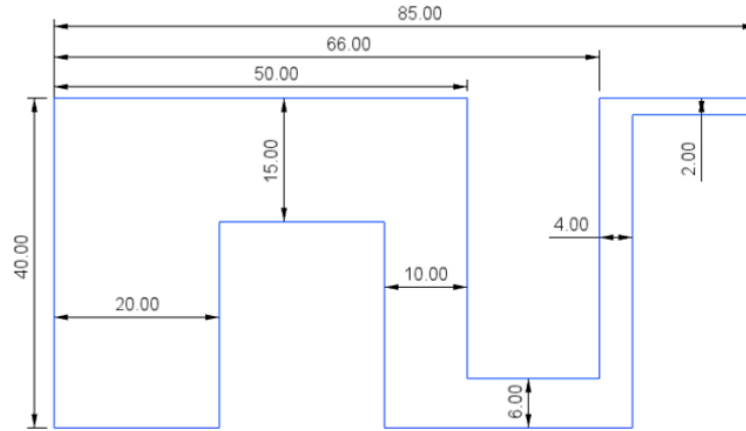
Figure 55 – Dimentions of the snake pattern used for half of the layer test.

This pattern was specifically designed to investigate the build plate adhesion of different sized areas as well as how the material interacts around corners. Here, we can pinpoint what sized areas do not have enough adhesion force to counteract warping. Also included is a single 10 mm x 10 mm x 2 mm box below the snake pattern. This was another area of interest in the formation of layers, but it also gave a glimpse into how the material handles printing multiple models at once.

Before layer testing was to commence, the data from section 4.1 was used to calibrate the printer. To skew the values from earlier testing, the printer settings were set to a the green nozzle (diameter at 0.8mm), a THV concentration of 4.5 g/ml, LW of 0.6 mm, LH of 0.2 mm, pressure of 9 PSI, and a speed of 4 mm/s. The serpentine pattern was printed using these skewed values (Figure 56). These settings created a print that did not have uniform lines. Seen widely throughout, there are areas of large waves where more material is being dispersed than needed. Also, there were signs of dragged material (white) in the center of the part. To combat the over-extrusion, we decided update the print parameters with the optimized values from section 4.1. The optimization was complete by increasing the speed to 10 mm/s,

decreasing the pressure to 8 psi, and increase the LH to 0.4 mm. The now optimized printer created a much smoother first layer in b). Each pass is distinctly marked by edged defined by darker shadows. The waviness seen in print a) is nonexistent in print b). Thus we claim that the calibration was a success.
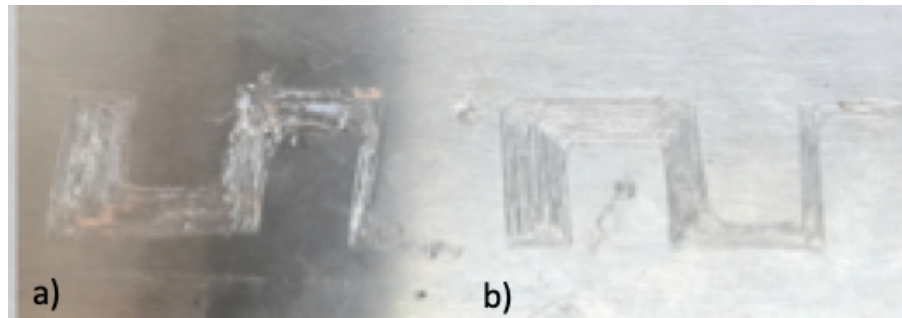
Figure 56 - Comparison between inadaquate single layer printing paramaters (a) with single layer calibrated paramaters (b).

We first decided to reprint the serpentine pattern at a single layer to double-check repeatability and our calibration. Once completed, we were confident in our calibration. We began another print, this time letting the print complete two layers of THV. This print is seen in Figure 57. Overall, the second layer of THV successfully created a distinct second layer above the first. Just like the first layer, each pass was clear, the bond to the second layer was laminated to the first, and there was no sign of warping.
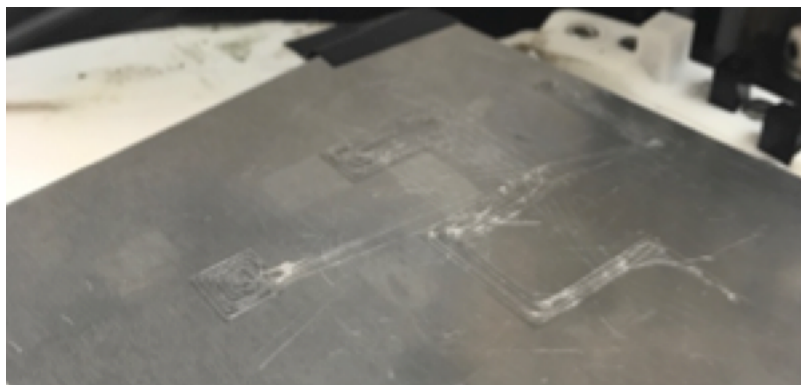
Figure 57 – Two layer serpentine print. No warpint was seen, but spiderwebbing is present.

Other than this success, there is a major observation not seen in previous layer tests. There is material drag moving from the serpentine pattern to the smaller printed box in the bottom left. This excess material, called spider webbing for its similar appearance, is a normally occurring phenomenon in the world of printing. In a blog post for the Ultimaker website, a leading brand of desktop printers, Lozova states that spiderwebbing is due to" small drops of material (that) ooze from the nozzle as it travels from one peak to the next" [28]. For a Pneumatic printer like the Biobot Basic, it is very logical that there may be residual pressures when switching between models. That by itself can create a small droplet within the nozzle, ready to be stretched. The fix for this is normally introducing a material retraction into the extruder, but this is very difficult to implement into a pneumatic system. Mechanical extruder heads have a stepper motor that has the ability to both push filament through the nozzle and pull it back into the nozzle. The Pneumatic pump installed into the Biobot Basic does not have the luxury of a reversible process. The pump has the ability to pressurize the syringe, but cannot create a negative pressure. Spider webbing does not interfere with the final products, so we treat it as part of the process.

A print of four layers was then commenced. This test proved to be the break point for warping (Figure 58), as the print curled everything but areas with a width of 20 mm and 15 mm. There was very little spider webbing in this print. It is interesting that the settings were the same and that both prints were completed one after another. Also, the smaller 10 mm x 10 mm square in the center left had no signs of warping. We theorize that the smaller 2 mm and 4 mm sections of the serpentine failed and curled up the 6 mm and 10mm sections.
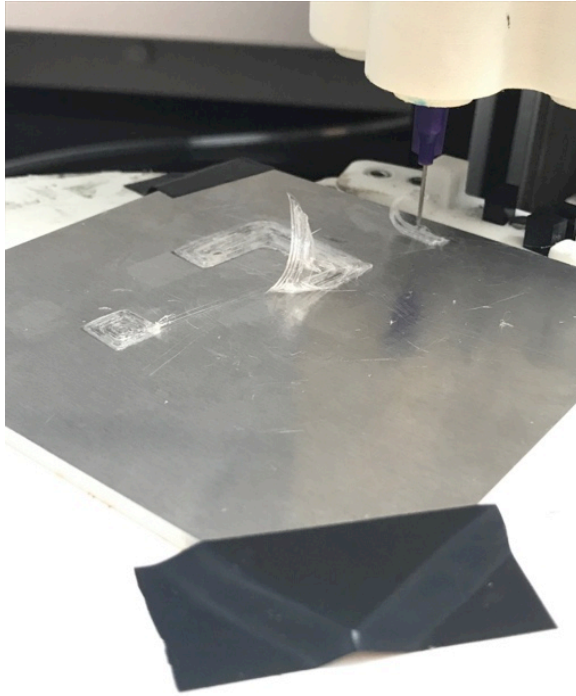
Figure 58 –THV warping at four layers.

It was then decided to remove the 2 mm, 4 mm, and 6 mm sections from the pattern to see if the 10 mm section sufficiently adheres to the bed. The 4 layer test was restarted. The model successfully print. No warping was observed in the 10 mm section, thus it can be concluded that the minimum width of a print with at least four layers is 10 mm across.
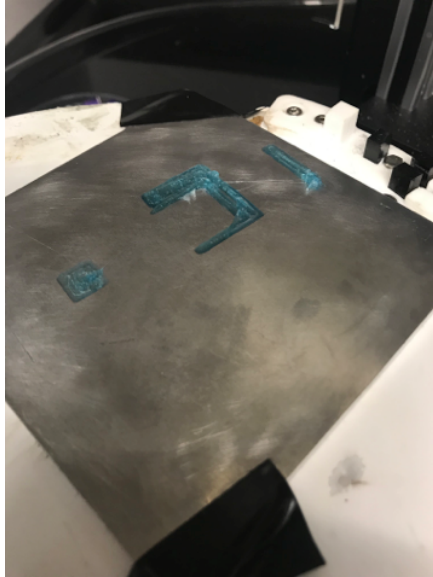
Figure 59 – Updated 4 layer THV experiment.

Chapter 5– Conclusions and Future Work

From this work, we explored the printing characteristics of GO aerogel and THV. In addition, we created a model to correlate the TSIM parameters to the fluid material parameters. The model and THV fluid characteristics can be found in Chapter 3. For future work, the model should be adjusted to include interference seen by Newtonian flow as well as any other friction values. This will greatly increase the accuracy of predicting the mass flow rate of the printer from the TSIM printing parameters.

The printing of GO Aerogel reported in this work is in the initial stages of development. The inadequate viscosity of the ink as well as the duality of the gelation method was difficult to control in initial testing. Thus, the material did not succeed to be repeatable nor be able to build layers. In its current form, GO Aerogel is not ready to be printed. It is hoped that the viscosity can be increased by the inclusion of binders or AL nanoparticles into the GO solution. A gel well may also be sought after as a print apparatus.

As a material with a higher viscosity, THV proved to be easily printable. The material was successful in its ability to create distinctive lines, print the same 5 mm^2 box with minimal geometric error, and support and bonding of multiple layers. Next steps for THV would be to compare the material with the inclusion of Aluminum nanoparticles, explore warping in greater detail, and expand to printing larger pieces.

REFERENCES

[1] Terry Wohlers and Tim Gornet, "History of Additive Manufacturing," Wohlers Associates, Wohlers Report 2014.

[2] (2015, March) University of Leeds Career Center Blog. [Online].   HYPERLINK "leedsunicareers.wordpress.com/2015/08/03/getting-into-the-3d-printing-industry/" leedsunicareers.wordpress.com/2015/08/03/getting-into-the-3d-printing-industry/

[3] D T Pham and S S Dimov, *Rapid Manufacturing: The Technologies and Applications of Rapid Prototyping*.: Springer-Verlag, 2001.

[4] Formlabs. (2017, June) formlabs.com. [Online].   HYPERLINK "formlabs.com/blog/what-is-selective-laser-sintering/"   formlabs.com/blog/what-is-selective-laser-sintering/

[5] Dana Goldberg. (2018, April) Autodesk.com. [Online].   HYPERLINK "autodesk.com/redshift/history-of-ed-printing/"   autodesk.com/redshift/history-of-ed-printing/

[6] Sean Aranda. (2015, July) SD3D. [Online].   HYPERLINK "sd3d.com/3d-printing-vs-injection-molding/"   sd3d.com/3d-printing-vs-injection-molding/

[7] Web of Science. Web of Science. [Online].   HYPERLINK "webofknowlege.com/RAMore.do?product=WOS&search_mode+GeneralSearch&SID=8AxeKFmCiZQ5X6FuV1u&qid=1&ra_mode" webofknowlege.com/RAMore.do?product=WOS&search_mode+GeneralSearch&SID=8AxeKFmCiZQ5X6FuV1u&qid=1&ra_mode

[8] Nadav Noor et al., "3D Printing of Personalized Thick and Perfusable Cardiac Patches and Hearts," *Advanced Sciences*, April 2019.

[9] Izabela Hager, Anna Golonka, and Roman Putanowicz, "3D Printing of Buildings and Building Components as the Future of Sustainable Construction?," *Procedia Engineering*, vol. 151, pp. 292-299, 2016.

[10] Press Release. (2010, October) NobelPrize.org. [Online].   HYPERLINK "www.nobelprize.org/prizes/physics/2010/press-release/" www.nobelprize.org/prizes/physics/2010/press-release/

[11] Nicola Lisi et al., "Contamination-free Graphene by Chemical Vapor Deposition in Quartz Furnaces," *Nature*, vol. 7, no. 7, August 2017.

[12] ACS Material LLC. (2017, November) ACS Material. [Online].   HYPERLINK "www.acsmaterial.com/blog/index/view/id/14/" www.acsmaterial.com/blog/index/view/id/14/

[13] Huitao Yu, Bangwen Zhang, Chaoke Bulin, Ruihong Li, and Ruiguang Xing, "High-efficient Synthesis of Graphene Oxide Besed on Improved Hummers Method," *Nature*, vol. 2016, no. 6, November 2016, doi: 10.1038/srep36142(2016).

[14] Rajagopalan Thiruvengadathan et al., "A Versatile Self-Assembly Approach towards High Performance Nanoenergetic Composite Using Functionalized Graphene," *Langmuir*, vol. 2014, no. 30, pp. 6556-6564, 2014.

[15] Anqi Wang et al., "Reactive Nanoenergetic Graphene Aerogel Synthesized by One-Step Chemical Reduction," Department of Biological Engineering, Department of Electrical and Computer Engineering, Department of Mechanical and Aerospace Engineering, University of Missouri - Columbai, Columbia,.

[16] Zhang Qiangqiang et al., "3D Printing of Graphene Aerogels," *Materials Views*, no. 13, pp. 1702-1708, February 2016.

[17] Polyfluor. (2019) Polyfluor. [Online].   HYPERLINK "polyfluor.ln/en/materials/thv/" polyfluor.ln/en/materials/thv/

[18] Byung-Doo Lee et al., "Ultra-rapid elimination of biofilms via the combustion of a nanoenergetic coating," *BMC Biotechnology*, vol. 13, no. 30, March 2013.

[19] Peter Smid, *CNC Programming Hndbook*, 3rd ed. New York, US: Industrual Press, 2008.

[20] Ed Tyson. rigid.ink. [Online].   HYPERLINK "rigid.ink/blogs/news/3d-prints-warping-why-it-happens-and-how-to-prevent-it"   rigid.ink/blogs/news/3d-prints-warping-why-it-happens-and-how-to-prevent-it

[21] Peter D. Olmsted and Claire Mcllroy, "Deformation of an amorphous polymer durring the fused-filament-fabrication method for additive manufacturing," *Journal of Rheology*, vol. 61, no. 2, p. 379, March 2017.

[22] (2019) Sigma aldrich. [Online].   HYPERLINK "www.sigmaaldrich/chemistry/stockroom-reagents/learning-center/technical-library/needle-gauge-chart.html"   www.sigmaaldrich/chemistry/stockroom-reagents/learning-center/technical-library/needle-gauge-chart.html

[23] James. (2011, April) blogspot.com. [Online].   HYPERLINK "adventuresin3-dprinting.blogspot.com/2011/04/calculating-flow-rate-value.html"   adventuresin3-dprinting.blogspot.com/2011/04/calculating-flow-rate-value.html

[24] Atta Sojoudi, Suvash C Saha, M A Hossain, and Y. T Gu, "Steady Naturla Convention of Non-Newtonian Power-Law Fluid in a Trapizodial Enclosure," *Advances in Mechanical Engineering*, vol. 2013, p. 8, January 2013.

[25] "Brookfield DV3T Viscometer Operating Instructions Manual N0. M13-2100-A0415," Brookfield, Middleboro, Manual.

[26] The Engineers Toolbox. [Online].   HYPERLINK "engineeringtoolbox.com/orifice-nozzle-venturi-d590.html"   engineeringtoolbox.com/orifice-nozzle-venturi-d590.html

[27] Monoprice. (2018, October) monoprice.com. [Online].   HYPERLINK "downloads.monoprice.com/files/manuals/13860_Manual151111.pdf" downloads.monoprice.com/files/manuals/13860_Manual151111.pdf

[28] Lana Lozova. (2016, October) Ultimaker. [Online].   HYPERLINK "ultimaker.com/en/blog/23426-seven-3d-printing-horror-stories-and-how-to-avoid-them"   ultimaker.com/en/blog/23426-seven-3d-printing-horror-stories-and-how-to-avoid-them